Sensitivity study of dimension-6 operators in the $W^{\pm}Z$ polarization phase space

Bachelor-Arbeit
zur Erlangung des Hochschulgrades
Bachelor of Science
im Bachelor-Studiengang Physik

vorgelegt von

Gregor Daberstiel
geboren am 22.10.2001 in Dresden

Institut für Kern- und Teilchenphysik
Fakultät Physik
Bereich Mathematik und Naturwissenschaften
Technische Universität Dresden
2023

Eingereicht am 6. Juni 2023

1. Gutachter: Dr. Frank Siegert
2. Gutachter: Prof. Dr. Arno Straessner

Abstract

English

Resulting from the Higgs mechanism of electroweak symmetry breaking in the standard model (SM) vector bosons (VB) gain mass and an additional degree of freedom in their possible polarization states. This third - longitudinal - polarization is inherently connected to the Higgs mechanism and opens the door for searches for possible new physics beyond the SM. A model independent approach to characterize deviations from the SM is Standard Model Effective Field Theory (SMEFT). It extends the SM by introducing higher dimension operators into the Lagrange density.
This thesis studies $W^{\pm}Z$ production processes in a phase space sensitive to VB polarization in the light of possible sensitivity to SMEFT contributions. Eight dimension 6 operators are separately simulated with the help of the event generator `SHERPA` at leading order with fully leptonic decay channels. Their influence on multiple observables at current Wilson coefficient bounds is assessed.
Even though further studies have to be conducted to better understand remaining issues connected to simulation of propagator contributions and closure between different contribution extraction approaches during the simulation of the SMEFT model, five of the eight studied operators show shape effect contributions in multiple observables. Fits of the operator contributions to the SM with basic binning led to tighter bounds on the Wilson coefficients of the $\mathcal{O}_{\varphi q3}$ and the $\mathcal{O}_{\tilde{W}}$ operators, suggesting sensitivity of the studied $W^{\pm}Z$ polarization phase space to SMEFT contributions. Tighter bound setting of more operators seems to be possible if more sophisticated binning and bin optimization methods were applied in the future.

Deutsch

Als Resultat des Higgs-Mechanismus der elektroschwachen Symmetriebrechung im Standardmodell (SM) erhalten Vektorbosonen (VB) Masse und einen zusätzliche Freiheitsgrad in ihren möglichen Polarisationszuständen. Diese dritte - longitudinale - Polarisation ist inhärent mit dem Higgs-Mechanismus verbunden und eröffnet die Möglichkeit, nach möglicher neuer Physik jenseits des SM zu suchen. Ein modellunabhängiger Ansatz zur Charakterisierung von Abweichungen vom SM ist die sogenannte SStandard Model Effective Field Theory"(SMEFT). Sie erweitert das SM durch die Einführung von Operatoren höherer Dimension in die Lagrangedichte.
Diese Arbeit untersucht die $W^{\pm}Z$-Produktionsprozesse im Phasenraum, der empfindlich für die VB-Polarisation ist, im Hinblick auf mögliche Sensitivität gegenüber SMEFT-Beiträgen. Acht Operatoren der Dimension 6 werden separat mit Hilfe des Ereignisgenerators `SHERPA` in führender Ordnung mit vollständig leptonischen Zerfallskanälen simuliert. Ihr Einfluss auf mehrere beobachtbare Größen bei aktuellen Grenzwerten der Wilson-Koeffizienten wird bewertet.
Obwohl weitere Studien durchgeführt werden müssen, um noch bestehende Probleme im Zusammenhang mit der Simulation von Propagatorbeiträgen und der Übereinstimmung zwischen verschiedenen Ansätzen zur Extraktion von Beiträgen während der Simulation des SMEFT-Modells besser zu verstehen, zeigen fünf der acht untersuchten Operatoren Beitragseffekte in mehreren beobachtbaren Größen. Ein Fit der Operatorbeiträge an das SM mit einfacher Binning-Methode führten zu engeren Grenzwerten für die Wilson-Koeffizienten der Operatoren $\mathcal{O}_{\varphi q3}$ und $\mathcal{O}_{\tilde{W}}$, was auf Sensitivität des untersuchten $W^{\pm}Z$-Polarisationsphasenraums gegenüber SMEFT-Beiträgen hindeutet. Eine genauere Grenzwertsetzung für weitere Operatoren scheint möglich zu sein, wenn in Zukunft Binoptimierungsmethoden angewendet werden.

Table of Content

1 Introduction

The standard model of particle physics (SM) is one of the most accurate and well tested theories in all of physics. With the discovery of the Higgs boson in 2012 [1] and the associated confirmation of the Higgs mechanism of electroweak symmetry breaking (EWSB), the latest piece has been added to the picture we have of the particle world. The model, however, remains incomplete. Only three of the four known fundamental forces are implemented into the theory. Gravity in its modern form of general relativity remains to be adapted into the framework of a quantum field theory (QFT) and its effects at large scales, especially those connected to dark matter and dark energy, remain unexplained. Experiments also showed deviations from theoretical calculations regarding the gyromagnetic ratio of the muon [2, 3]. In light of those observed phenomena further and more accurate measurements have to be conducted to probe the SM and find possible new physics beyond our current understanding. One of the tools at a physicist's disposal is the Large Hadron Collider (LHC) at CERN, whose four primary experiments ATLAS, CMS, ALICE and LHCb already showed great success in, for example, helping to discover the aforementioned Higgs boson. The data acquired during the particle collisions may show further deviations from the SM and shed light on possible new theories beyond the SM (BSM). A promising possibility amongst the wide variety of possible processes is vector boson scattering (VBS) in which two or more vector bosons (VB) interact with each other via multiple possible gauge couplings. Because of VB properties resulting from electroweak symmetry breaking and its effects on possible polarization states of the particles it is a perfect candidate to probe not only the SM but especially the contained Higgs mechanism and find possible new physics connected to it. Since these processes are quite rare, the focus of this thesis will be diboson processes which exhibit similar final states and properties as VBS processes. One of way to quantify deviations from the SM is the effective field theory (EFT) approach. It parameterizes deviations from the SM stemming from resonances beyond the energy scale which is currently reachable in experiments. To study these processes simulations with different EFT operators are performed.

Using the Monte-Carlo event generator `SHERPA` different models will be simulated, which can later be analyzed and discussed.
The goal of this study is to test a phase space currently being investigated at ATLAS in relation to VB polarization for its sensitivity to selected EFT operators and set bounds on the Wilson coefficients accompanying the operators. For this purpose, in the first part of this thesis, the necessary theoretical and experimental foundations are laid. Subsequently, in the second part, the explicit implementation in `SHERPA` is discussed.

2 Theoretical Background

2.1 The Standard Model

This chapter is based upon the content of [4]. A full introduction to the SM, its effects and additional caveats not discussed in this chapter can also be found there.
The foundational model which modern particle physics is built upon is the SM. It is able to describe three of the four known fundamental interactions: The electromagnetic and the weak interaction, which combine to the electroweak (EW) interaction through the Higgs mechanism, and the strong interaction. The description is based upon local gauge symmetries which can be expressed in a fairly condensed notation as

$$\mathrm{U}(1)_Y \otimes \mathrm{SU}(2)_L \otimes \mathrm{SU}(3)_C, \tag{2.1}$$

utilizing the mathematical framework of group theory. The first two terms in the tensor product refer to the EW interaction in the form of the unitary group of degree one $\mathrm{U}(1)_Y$ and special unitary group of degree two $\mathrm{SU}(2)_L$. The last term is related to the strong interaction in the form of the special unitary group of degree three $\mathrm{SU}(3)_C$.
To each of these Lie groups there are associated generators that span the tangent space of the underlying Lie manifold. To every one of those operators corresponds a force carrying gauge boson with integer spin. The fundamental forces which are already incorporated into the theory are mediated by vector bosons with spin 1. For electromagnetism this is the photon γ, for the strong interaction exist eight gluons g and the weak interaction is mediated by the Z and $W^{\pm}$ boson. Additionally to the vector bosons there exists a spin 0 scalar boson H that results from the Higgs mechanism of electroweak symmetry breaking (EWSB) which is discussed in Section 2.1.1. The full set of SM bosons and their charges can be found in Table 2.2.
Besides the bosonic part of the SM, there exist four different classes divided into

three (known) generations of elementary fermions. These, depending on their charges with respect to the fundamental forces, interact with the gauge bosons. There are the quarks, which have a non-zero color charge and thus can interact with the strong force. Due to their differing weak isospin they form a weak isospin doublet, splitting into the sub classes of up and down type quarks and therefore also interact with the weak force. Through their nonzero electric charge they also interact with the electromagnetic force. Then there are the leptons which, through weak isospin, again split into an isospin doublet of electromagnetically charged leptons, e.g. the electron e, and uncharged leptons, e.g. the electron neutrino ν_e. Both interact with the weak force, but only the electromagnetically charged leptons interact with the electromagnetic force.
It was first shown by the Wu experiment [5] that only left-handed particles (and right-handed antiparticles) interact with the weak force making the SM a chiral theory. The full set of SM fermions and their charges can be found in Table 2.1.

2.1.1 The Higgs Mechanism

Following the EW symmetry part of the SM before EWSB,

$$\mathrm{U}(1)_Y \otimes \mathrm{SU}(2)_L \tag{2.2}$$

the gauge bosons that mediate these interactions should be massless since massive terms like $\frac{1}{2}m_\gamma A_\mu A^\mu$ in the Lagrange density that transform under U(1) like $A_\mu \rightarrow A_\mu = A_\mu - \partial_\mu \chi$ are inherently not locally gauge invariant:

$$\frac{1}{2}m_\gamma A_\mu A^\mu \rightarrow \frac{1}{2}m_\gamma (A_\mu - \partial_\mu \chi)(A^\mu - \partial^\mu \chi) \neq \frac{1}{2}m_\gamma A_\mu A^\mu \tag{2.3}$$

While the photon follows this principle, the $W^\pm$ and Z boson have been observed to be massive [6, 7] and therefore stand in stark contrast to the prediction of this version of the SM.
The solution to this conundrum lies in the introduction of a complex scalar field which interacts with particles and generates the described mass terms in the Lagrange density for the massive particles. A complex field

$$\phi = \frac{1}{\sqrt{2}}(\phi_1 + i\phi_2) \tag{2.4}$$

with its Lagrange density

$$\mathcal{L} = \frac{1}{2}\left(\partial_\mu\phi_1\right)\left(\partial^\mu\phi_1\right) + \frac{1}{2}\left(\partial_\mu\phi_2\right)\left(\partial^\mu\phi_2\right) - \frac{1}{2}\mu^2\left(\phi_1^2 + \phi_2^2\right) - \frac{1}{4}\lambda\left(\phi_1^2 + \phi_2^2\right)^2 \tag{2.5}$$

is introduced which for values $\lambda > 0$ and $\mu^2 \in \mathbb{R}$ has a finite minimum. If $\mu^2 \geq 0$ the minimum occurs at the origin $\phi_1, \phi_2 = 0$. For $\mu^2 < 0$ the potential assumes its minimal value within the infinite set defined by

$$\phi_1^2 + \phi_2^2 = \frac{-\mu^2}{\lambda} := v^2 \tag{2.6}$$

where v is the vacuum expectation value (Vev). By choosing one of these minima, the global U(1) symmetry is spontaneously broken. Transforming into coordinates such that $(\phi_1, \phi_2) = (v, 0)$ and expanding around the Vev such that $\phi = \frac{1}{\sqrt{2}}(\eta + v + i\xi)$ the Lagrange density can be rewritten as

$$\mathcal{L} = \frac{1}{2}\left(\partial_\mu\eta\right)\left(\partial^\mu\eta\right) - \frac{1}{2}m_\eta^2\eta^2 + \frac{1}{2}\left(\partial_\mu\xi\right)\left(\partial^\mu\xi\right) - V_{\text{interaction}} \tag{2.7}$$

with $m_\eta = \sqrt{2\lambda v^2}$ and

$$V_{\text{interaction}} = \lambda v\eta^3 + \frac{1}{4}\lambda\eta^4 + \frac{1}{4}\lambda\xi^3 + \lambda v\eta\xi^2 + \frac{1}{2}\lambda\eta^2\xi^2 \tag{2.8}$$

where a mass term m_η is generated and triple and quartic self couplings between the η and ξ fields emerge in the interaction potential $V_{\text{interaction}}$. The excitations of η and ξ play different roles: Whereas ξ is a (virtual) Goldstone boson in the direction in which the field is invariant and thus can be gauged by the right transformation, the massive η is physical and a result of the symmetry breaking through the choice of a specific ground state.

For a SM-like U(1) invariant theory with subsequent field B_μ and coupling constant g and field strength tensor $F^{\mu\nu} = \partial^\mu B^\nu - \partial^\nu B^\mu$ one needs to replace the derivative operators ∂_μ with covariant derivatives $D_\mu = \partial_\mu + igB_\mu$ and include the gauge fields in the Lagrange density, leading to

$$\mathcal{L} = -\frac{1}{4}F^{\mu\nu}F_{\mu\nu} + (D_\mu\phi)^*(D^\mu\phi) - \mu^2\phi^2 - \lambda\phi^4 \tag{2.9}$$

Expanding Equation (2.9), breaking the symmetry with $\mu^2 < 0$ as done before without the fields and eliminating ξ by choosing an appropriate gauge yields

$$\mathcal{L} = \frac{1}{2}\left(\partial_\mu \eta\right)\left(\partial^\mu \eta\right) - \frac{1}{2}m_\eta^2\eta^2 - \frac{1}{4}F^{\mu\nu}F_{\mu\nu} + \frac{1}{2}g^2v^2B_\mu B^\mu - V_{\text{interaction}}(\eta, B^\mu) \tag{2.10}$$

where $V_{\text{interaction}}$ includes multiple interaction terms between the fields. By this process, not only a mass term for η but also for B^μ emerges, making the corresponding gauge boson massive.

It has to be noted that through the process of symmetry breaking additional physical degrees of freedom emerge. From the initial four degrees of freedom (η , ξ and two polarizations from B_μ) only one is found in the gauge transformation that eliminated the Goldstone boson ξ. As a direct result of a massive gauge boson another degree of freedom arises, which can be interpreted as a third - longitudinal - polarization. This will be discussed further in Section 2.1.3.

The last step to going from the toy model to the implementation of EWSB into the SM is to not only consider a breaking of $\mathrm{U}(1)_Y$ but of the full $\mathrm{U}(1)_Y \otimes \mathrm{SU}(2)_L$. The model then is comprised of two complex scalar fields placed inside of a weak isospin doublet. Following similar arguments as before the scalar field, after symmetry breaking and gauging three Goldstone fields, can be rewritten as

$$\phi(x) = \frac{1}{\sqrt{2}}\begin{pmatrix}\phi_1 + i\phi_2 \\ \phi_3 + i\phi_4\end{pmatrix} \longrightarrow \frac{1}{\sqrt{2}}\begin{pmatrix}0 \\ v + h(x)\end{pmatrix} \tag{2.11}$$

After introducing the covariant derivative for the $\mathrm{U}(1)_Y \otimes \mathrm{SU}(2)_L$

$$D_\mu = \partial_\mu + ig_{\mathrm{W}}\frac{1}{2}\left(\boldsymbol{\sigma}\cdot\boldsymbol{W}\right)_\mu + ig'\frac{1}{2}YB_\mu \tag{2.12}$$

mass is generated by terms generated through $(D_\mu\phi)^\dagger(D^\mu\phi)$. Expanding the terms and through comparing coefficients of those quadratic in the gauge fields

$$\frac{v^2}{8}g_{\mathrm{W}}^2(W_\mu^{(1)}W^{(1)\mu} + W_\mu^{(2)}W^{(2)\mu}) + \frac{v^2}{8}(g_{\mathrm{W}}W_\mu^{(3)} - g'B_\mu)(g_{\mathrm{W}}W^{(3)\mu} - g'B^\mu) \tag{2.13}$$

the masses in front of the kinetic terms can be read off, yielding

$$m_W = \frac{1}{2} g_W v \tag{2.14}$$

for the mass of the $W^{\pm}$ bosons taken from the first term. The second term is not diagonal in the fields $W^{(3)}$ and B, making it necessary to diagonalize it. This results in the (mass) eigenvalues

$$m_\gamma = 0 \tag{2.15}$$

$$m_Z = \frac{v}{2}\sqrt{(g_W^2 + g'^2)} \tag{2.16}$$

and its physical fields A_μ and Z_μ as eigenstates

$$\begin{pmatrix} A^\mu \\ Z^\mu \end{pmatrix} = \frac{1}{\sqrt{(g_W^2 + g'^2)}} \begin{pmatrix} g' W_\mu^{(3)} + g_W B_\mu \\ g_W W_\mu^{(3)} - g' B_\mu \end{pmatrix} \tag{2.17}$$

Thus, after EWSB, the gauge bosons $W^{\pm}$ and Z of the weak interaction have acquired mass as well as an additional degree of freedom in the form of a longitudinal polarization while the photon γ remains massless with its familiar two transverse polarization states.
A more detailed derivation and discussion of the Higgs mechanism and its further effects, like the Yukawa mechanism for fermion masses, can be found in [4, 8, 9].

With this mechanism the SM arrives at its current form with its set of particles and their respective charges found in Table 2.1 and Table 2.2.

2.1.2 $W^{\pm}Z$ Production Processes

Probing the SM for deviations is particularly interesting in the EW sector, since it is inherently connected to the EWSB and is therefore a promising starting point to search for new physics. One of the most interesting processes to investigate is the $W^{\pm}Z$ production process due to the possibility of $W^{\pm}W^{\pm}Z$ triple gauge coupling at the leading order (LO) with 4 EW vertices. It thus makes for an interesting candidate to study the gauge structure of the SM on the one hand as well as a wide variety of properties like polarization on the other. The contributing diagrams at LO are shown in Figure 2.1. In practice at the LHC at LO the involved annihilating

Table 2.1: Fermions of the SM. Weak isospin is 0 for all right-handed particles. Masses are taken from [10].

Type	Particle	Gen.	Color	Electric Charge	Weak Isospin LH	Mass
Quarks	up u	1	yes	2/3	1/2	2.2 MeV
	down d	1	yes	- 1/3	- 1/2	4.7 MeV
	charm c	2	yes	2/3	1/2	1.28 GeV
	strange s	2	yes	- 1/3	- 1/2	96 MeV
	top t	3	yes	2/3	1/2	173.1 GeV
	bottom b	3	yes	- 1/3	- 1/2	4.18 GeV
Leptons	electron e	1	no	-1	- 1/2	0.511 MeV
	muon μ	2	no	-1	- 1/2	105.66 MeV
	tauon τ	3	no	-1	- 1/2	1.7768 GeV
	electron neutrino ν_e	1	no	0	1/2	<1.1 eV
	muon neutrino ν_μ	2	no	0	1/2	< 0.19 MeV
	tauon neutrino ν_τ	3	no	0	1/2	<18.2 MeV

Table 2.2: Bosons of the SM. Masses are taken from [10].

Type	Particle	Color	Electric Charge	Weak Isospin	Mass
Vector Bosons	photon γ	no	0	0	0 eV
	gluon g	yes	0	0	0 eV
	$W^\pm$ boson	no	$\pm$ 1	$\pm$ 1	80.377 GeV
	Z boson	no	0	0	91.1876 GeV
Scalar Bosons	Higgs boson H	no	0	- 1/2	125.25 GeV

quarks in the initial state are an $u\bar{d}$ pair for W^+Z and $d\bar{u}$ for W^-Z production. The bosons decay either into a fermion-anti fermion pair in case of the Z boson or into a lepton and an antineutrino or a quark and an anti isospin-partner pair in case of the $W^\pm$ boson [11]. In this thesis, only the leptonic decay channels are considered since they are easier to reconstruct and show only small backgrounds because of missing hadronic jets.

Figure 2.1: LO diagrams for the $W^{\pm}Z$ diboson process with fully leptonic final states

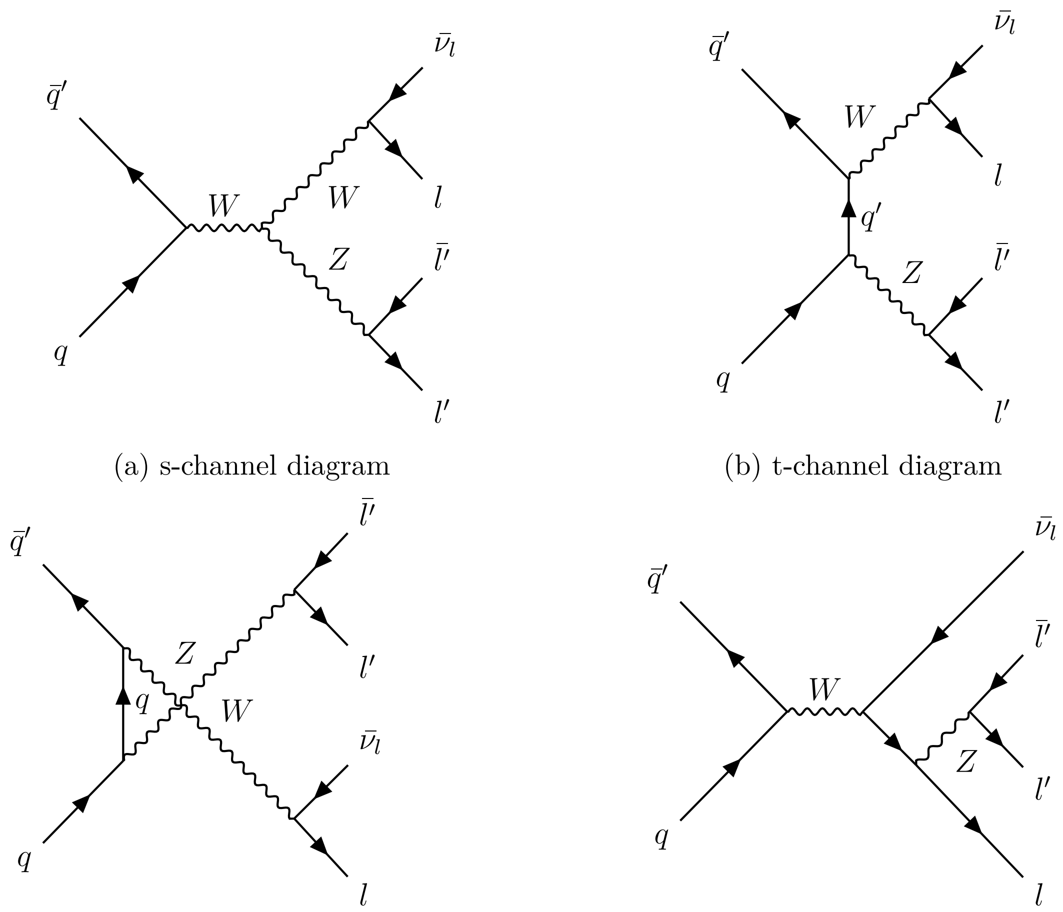

(a) s-channel diagram (b) t-channel diagram

(c) u-channel diagram (d) radiative diagram

2.1.3 Vector Boson polarization

The helicity operator is defined as the projection of the spin $\vec{S}$ onto the particles direction of motion $\frac{\vec{p}}{p}$

$$H = \vec{S} \cdot \frac{\vec{p}}{p} \tag{2.18}$$

Massive spin 1 particles can have three different helicity eigenvalues $h \in \{\pm 1, 0\}$. In the case of a massless boson, there is no way to transform into the rest frame of said particle and therefore the helicity 0 state vanishes. Mathematically, this is the result of a freedom of choice of a gauge in the plane wave equation for the photon field.

For massive particles, the helicity operator is not Lorentz invariant due to different treatment of three-momentum and energy. Therefore, for massive spin 1 particles a reference frame has to be chosen for a unambiguous definition of polarization. As one of the effects of EWSB, the $W^{\pm}$ and Z bosons gain mass. An interesting consequence of this is the introduction of a third - longitudinal - polarization degree of freedom, as discussed in Section 2.1.1, corresponding to the $h = 0$ eigenvalue of the helicity operator. The remaining two transverse polarization directions, which correspond to the $h = \pm 1$ eigenvalues, are present in both massive and massless bosons. These polarization states are described by the polarization vectors ε_μ which for $\vec{p} = p\hat{z}$ can be written as

$$\text{Transverse: } \epsilon_\mu(\pm 1) = \frac{1}{\sqrt{2}} \begin{pmatrix} 0 \\ \pm 1 \\ -i \\ 0 \end{pmatrix} \qquad \text{Longitudinal: } \epsilon_\mu(0) = \frac{1}{m} \begin{pmatrix} p \\ 0 \\ 0 \\ E \end{pmatrix} \tag{2.19}$$

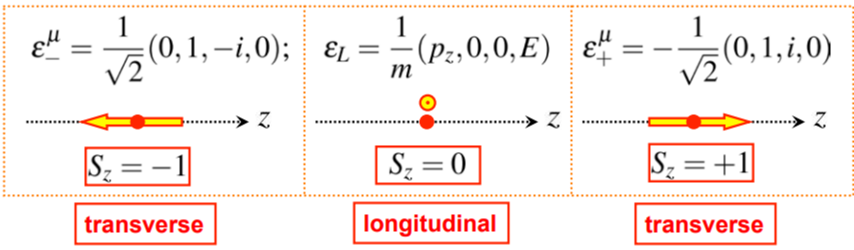

Figure 2.3: The three possible helicity eigenvalues of massive vector bosons with the corresponding polarization vectors. From [12].

The differential cross section can be expressed as a function of the polarization fractions f_{L} f_{R}, denoting the fraction of left and right handed transversal polarizations and f_0 the longitudinal polarization respectively. For massless fermions in the rest frame of the parent $W^{\pm}$ boson the angular cross section distribution is then given by

$$\begin{aligned} \frac{1}{\sigma_{W^{\pm}Z}} \frac{d\sigma_{W^{\pm}Z}}{d\cos\theta^{\mathbf{WZ\ into\ W}}_{W\ \mathrm{Lep}}} &= \frac{3}{8} f_{\mathrm{L}} (1 \mp \cos\theta^{\mathbf{WZ\ into\ W}}_{W\ \mathrm{Lep}})^2 \\ &+ \frac{3}{8} f_{\mathrm{R}} (1 \pm \cos\theta^{\mathbf{WZ\ into\ W}}_{W\ \mathrm{Lep}})^2 \\ &+ \frac{3}{4} f_0 \sin^2\theta^{\mathbf{WZ\ into\ W}}_{W\ \mathrm{Lep}} \end{aligned} \tag{2.20}$$

as discribed in Ref. [13].

2.2 Effective Field Theory

There are many approaches to search for new physics beyond the SM (BSM). Direct measurements of particle resonances at the current collision energies or even deviations in the high-energy tail for an explicit BSM theory are one way to measure new particles and its corresponding interactions. This approach has the disadvantage of only testing one specific theory and not a wide variety of possible new theories whose effects all might lead to a similar deviation. A more general approach and therefore a commonly more popular method is the effective field theory (EFT) approach which for the SM is called Standard Model effective field theory (SMEFT). Knowing the Lagrange density of the SM one can try to parameterize small deviations from the expected theory in terms of new higher order operators with the help of coupling coefficients. These deviations can only accurately describe resonances which are beyond the collision energy of our current detectors, meaning that only tail end resonance effects should be visible in current experiments which can then be parameterized with SMEFT (Figure 2.4). This

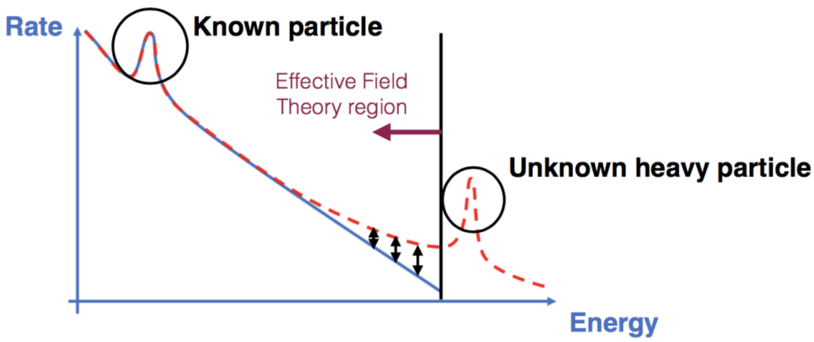

Figure 2.4: Schematic idea of SMEFT. The vertical line represents the SMEFT cutoff [14]

leads to a series expansion

$$\mathcal{L}_{\text{SMEFT}} = \mathcal{L}_{\text{SM}} + \frac{1}{\Lambda} c^{(5)} \mathcal{O}^{(5)} + \frac{1}{\Lambda^2} \sum_i c_i^{(6)} \mathcal{O}_i^{(6)} + \sum_{k \geq 8} \frac{1}{\Lambda^k} \sum_j c_j^{(k)} \mathcal{O}_j^{(k)} \tag{2.21}$$

where the $O_j^{(k)}$ are the possible dimension k operators, the $c_j^{(k)}$ are the so-called Wilson coefficients coupling the Operators to the SM. Λ is the SMEFT energy cutoff which introduces the energy scale at which the operators become relevant. The SM is then recovered as the low energy limit of the SMEFT theory.

The possible operators are a composition of differential, fermionic and bosonic operators, which combine to an operator with a dimension higher than those in the dimension four SM. In this thesis, only dimension 6 operators will be considered. As members of a linear vector space the operators can be written in different bases. The most common basis used to study dim-6 SMEFT models is the Warsaw basis [15, 16], which was also used in this thesis. All operators then result in corrections

X^3		φ^6 and $\varphi^4 D^2$		$\psi^2\varphi^3$	
Q_G	$f^{ABC} G_\mu^{A\nu} G_\nu^{B\rho} G_\rho^{C\mu}$	Q_φ	$(\varphi^\dagger\varphi)^3$	$Q_{e\varphi}$	$(\varphi^\dagger\varphi)(\bar{l}_p e_r \varphi)$
$Q_{\widetilde{G}}$	$f^{ABC} \widetilde{G}_\mu^{A\nu} G_\nu^{B\rho} G_\rho^{C\mu}$	$Q_{\varphi\Box}$	$(\varphi^\dagger\varphi)\Box(\varphi^\dagger\varphi)$	$Q_{u\varphi}$	$(\varphi^\dagger\varphi)(\bar{q}_p u_r \widetilde{\varphi})$
Q_W	$\varepsilon^{IJK} W_\mu^{I\nu} W_\nu^{J\rho} W_\rho^{K\mu}$	$Q_{\varphi D}$	$\left(\varphi^\dagger D^\mu\varphi\right)^\star \left(\varphi^\dagger D_\mu\varphi\right)$	$Q_{d\varphi}$	$(\varphi^\dagger\varphi)(\bar{q}_p d_r \varphi)$
$Q_{\widetilde{W}}$	$\varepsilon^{IJK} \widetilde{W}_\mu^{I\nu} W_\nu^{J\rho} W_\rho^{K\mu}$				
$X^2\varphi^2$		$\psi^2 X\varphi$		$\psi^2\varphi^2 D$	
$Q_{\varphi G}$	$\varphi^\dagger\varphi\, G_{\mu\nu}^A G^{A\mu\nu}$	Q_{eW}	$(\bar{l}_p\sigma^{\mu\nu} e_r)\tau^I\varphi W_{\mu\nu}^I$	$Q_{\varphi l}^{(1)}$	$(\varphi^\dagger i\overleftrightarrow{D}_\mu\varphi)(\bar{l}_p\gamma^\mu l_r)$
$Q_{\varphi\widetilde{G}}$	$\varphi^\dagger\varphi\, \widetilde{G}_{\mu\nu}^A G^{A\mu\nu}$	Q_{eB}	$(\bar{l}_p\sigma^{\mu\nu} e_r)\varphi B_{\mu\nu}$	$Q_{\varphi l}^{(3)}$	$(\varphi^\dagger i\overleftrightarrow{D}_\mu^I\varphi)(\bar{l}_p\tau^I\gamma^\mu l_r)$
$Q_{\varphi W}$	$\varphi^\dagger\varphi\, W_{\mu\nu}^I W^{I\mu\nu}$	Q_{uG}	$(\bar{q}_p\sigma^{\mu\nu} T^A u_r)\widetilde{\varphi}\, G_{\mu\nu}^A$	$Q_{\varphi e}$	$(\varphi^\dagger i\overleftrightarrow{D}_\mu\varphi)(\bar{e}_p\gamma^\mu e_r)$
$Q_{\varphi\widetilde{W}}$	$\varphi^\dagger\varphi\, \widetilde{W}_{\mu\nu}^I W^{I\mu\nu}$	Q_{uW}	$(\bar{q}_p\sigma^{\mu\nu} u_r)\tau^I\widetilde{\varphi}\, W_{\mu\nu}^I$	$Q_{\varphi q}^{(1)}$	$(\varphi^\dagger i\overleftrightarrow{D}_\mu\varphi)(\bar{q}_p\gamma^\mu q_r)$
$Q_{\varphi B}$	$\varphi^\dagger\varphi\, B_{\mu\nu} B^{\mu\nu}$	Q_{uB}	$(\bar{q}_p\sigma^{\mu\nu} u_r)\widetilde{\varphi}\, B_{\mu\nu}$	$Q_{\varphi q}^{(3)}$	$(\varphi^\dagger i\overleftrightarrow{D}_\mu^I\varphi)(\bar{q}_p\tau^I\gamma^\mu q_r)$
$Q_{\varphi\widetilde{B}}$	$\varphi^\dagger\varphi\, \widetilde{B}_{\mu\nu} B^{\mu\nu}$	Q_{dG}	$(\bar{q}_p\sigma^{\mu\nu} T^A d_r)\varphi\, G_{\mu\nu}^A$	$Q_{\varphi u}$	$(\varphi^\dagger i\overleftrightarrow{D}_\mu\varphi)(\bar{u}_p\gamma^\mu u_r)$
$Q_{\varphi WB}$	$\varphi^\dagger\tau^I\varphi\, W_{\mu\nu}^I B^{\mu\nu}$	Q_{dW}	$(\bar{q}_p\sigma^{\mu\nu} d_r)\tau^I\varphi\, W_{\mu\nu}^I$	$Q_{\varphi d}$	$(\varphi^\dagger i\overleftrightarrow{D}_\mu\varphi)(\bar{d}_p\gamma^\mu d_r)$
$Q_{\varphi\widetilde{W}B}$	$\varphi^\dagger\tau^I\varphi\, \widetilde{W}_{\mu\nu}^I B^{\mu\nu}$	Q_{dB}	$(\bar{q}_p\sigma^{\mu\nu} d_r)\varphi\, B_{\mu\nu}$	$Q_{\varphi ud}$	$i(\widetilde{\varphi}^\dagger D_\mu\varphi)(\bar{u}_p\gamma^\mu d_r)$

Figure 2.5: Boson-including dim-6 operators in the Warsaw basis

to existing or completely new vertices and Feynman rules. The final matrix element for a single dim-6 Operator can then be written as

$$|\mathcal{M}_{\text{SMEFT}}|^2 = |\mathcal{M}_{\text{SM}}|^2 + \frac{2c}{\Lambda^2}\,|\mathcal{M}_{\text{SM}}\mathcal{M}_{\text{Operator}}| + \frac{c^2}{\Lambda^4}\,|\mathcal{M}_{\text{Operator}}|^2 \tag{2.22}$$

which results in the cross section contribution

$$\sigma_{\text{SMEFT}} = \sigma_{\text{SM}} + c\sigma_{\text{linear}} + c^2\sigma_{\text{quadratic}} \tag{2.23}$$

For two choices of the Wilson coefficient there is effectively no contribution to the cross section: Either the coefficient is zero outright or the contributions linear and quadratic in the new operator matrix element exactly cancel out leaving no observable cross section contribution.

$$c = 0 \tag{2.24}$$

$$c = -2\Lambda^2 \frac{\sigma_{\text{linear}}}{\sigma_{\text{quadratic}}} \tag{2.25}$$

One successful application of this formalism was the Fermi coupling for the weak force in β decay before the discovery of the $W^{\pm}$ boson. The relevant SM interactions are

$$\mathcal{L} = \frac{g_w}{\sqrt{2}} \left(d\bar{\sigma}_\rho \bar{u} + \bar{\nu}_e \bar{\sigma}_\mu u \right) \mathrm{W}_\mu^- + \text{h.c.} \tag{2.26}$$

and the resulting matrix element at LO is proportional to

$$\mathcal{M} \propto \frac{1}{q^2 - m_W^2} \tag{2.27}$$

with the $W^{\pm}$ mass

$$m_W = 80 \text{ GeV}. \tag{2.28}$$

Since the $W^{\pm}$ boson has a high mass, its propagator can, at low energies $q^2 \ll m_W^2$, be approximated with

$$M \propto -\frac{1}{m_W^2} \tag{2.29}$$

which leads to an effective theory

$$\mathcal{L}_{\text{Effective}} = \frac{c}{\Lambda^2} \left(d\bar{\sigma}_\rho \bar{u} \right) \left(\bar{\nu}_e \bar{\sigma}_\rho e \right) \tag{2.30}$$

where at one vertex effectively four fermions interact (see Figure 2.6). The Wilson coefficient c and cutoff Λ can then be matched to be

$$\Lambda = m_W, \qquad c = -\frac{g_W^2}{2} \tag{2.31}$$

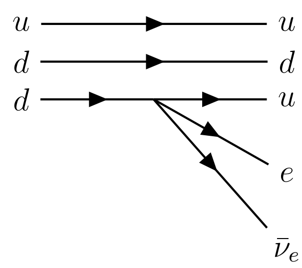

Figure 2.6: Effective β^- decay

2.2.1 Relevant Operators

The relevant operators that could contribute to the $W^{\pm}Z$ production at LO are listed below with their theoretical contributions. The exact contribution values can be acquired from [17].

1. $\mathcal{O}_{\mathrm{uW}}$: all channels, new diagram Figure 2.7
2. $\mathcal{O}_{\mathrm{dW}}$: all channels, new diagram Figure 2.7
3. $\mathcal{O}_{\varphi\mathrm{ud}}$: all channels
4. $\mathcal{O}_{\varphi\mathrm{u}}$: u channel
5. $\mathcal{O}_{\varphi\mathrm{d}}$: t channel
6. $\mathcal{O}_{\varphi\mathrm{e}}$: all channels
7. $\mathcal{O}_{\varphi\mathrm{q1}}$: t, u channels
8. $\mathcal{O}_{\varphi\mathrm{q3}}$: all channels
9. $\mathcal{O}_{\varphi\mathrm{l1}}$: all channels
10. $\mathcal{O}_{\varphi\mathrm{l3}}$: all channels
11. $\mathcal{O}_{\mathrm{uB}}$: u channel
12. $\mathcal{O}_{\mathrm{dB}}$: t channel
13. $\mathcal{O}_{\mathrm{eW}}$: all channels
14. $\mathcal{O}_{\mathrm{eB}}$: all channels
15. $\mathcal{O}_{\varphi\mathrm{WB}}$: all channels
16. $\mathcal{O}_{\varphi\tilde{\mathrm{W}}\mathrm{B}}$: s, radiative channel
17. $\mathcal{O}_{\mathrm{W}}$: s, radiative channels
18. $\mathcal{O}_{\tilde{\mathrm{W}}}$: s, radiative channel
19. $\mathcal{O}_{\varphi\mathrm{D}}$: Z mass and propagator

The $\mathcal{O}_{\mathrm{uW}}$ and $\mathcal{O}_{\mathrm{dW}}$ are particularly interesting since they introduce another tree level diagram through a quartic vertex. Even though the $\mathcal{O}_{\varphi\mathrm{D}}$ operator does not by itself introduce a vertex or a contribution to one, it does contribute to the Z mass and therefore its propagator [18]. These propagator changes as well as changes in the coupling constants $\bar{g}$ and $\bar{g}'$ are the case for other operators as well.

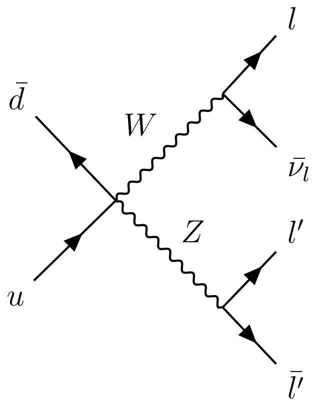

Figure 2.7: Quartic vertex that leads to new diagram

$$\bar{g} = \frac{g}{1 - \mathrm{C}_{\varphi\mathrm{W}} v^2} \tag{2.32}$$

$$\bar{g}' = \frac{g}{1 - \mathrm{C}_{\varphi\mathrm{B}} v^2} \tag{2.33}$$

$$\mathrm{M_W} = \frac{1}{2}\bar{g}v \tag{2.34}$$

$$\mathrm{M_Z} = \frac{1}{2}\sqrt{\bar{g}^2 + \bar{g}'^2}\, v \left(1 + \frac{\mathrm{C}_{\varphi\mathrm{WB}} v^2 \bar{g}\bar{g}'}{\bar{g}^2 + \bar{g}'^2}\right)\left(1 + \frac{\mathrm{C}_{\varphi\mathrm{D}} v^2}{4}\right) \tag{2.35}$$

3 Experimental Setup

In order to test the predictions made by the SM an experimental setup is needed that is capable of observing very rare scattering events with low cross sections. One of the experiments built to satisfy these criteria is the Large Hadron Collider (LHC) at CERN. The LHC is a high energy circular collider in the vicinity of Geneva which was built by a multinational collaboration and first put into commission in 2010 with a centre of mass energy (CME) of 7 TeV. After several upgrades in past years the so-called Run 3 started in 2022 at the current CME of 13.6 TeV. It is built upon the preexisting infrastructure of the Large Electron Positron Collider (LEP). The protons are guided around the 26.7 km long LHC accelerator ring by the use of liquid helium cooled superconducting magnets which hold the particle bunches in their circular paths and focus the beams to achieve a peak luminosity of $L = 10^{34}\ \frac{1}{\mathrm{cm}^2\mathrm{s}}$ at ATLAS and CMS - two of many experiments conducted at LHC. [19]. An overview over the ATLAS detector will be given in section 3.1.
Improving our understanding of the lesser tested parts of the SM, like for example the Higgs mechanism and its consequences, is often hard to achieve using experimental data alone. To be able to test those most improbable processes reliably and compare measurements to the theoretical predictions, event simulations have to be involved. Generating events based on a given theory by the means of Monte-Carlo methods (MC) can either shine a light on processes or observables that might be of interest for further studies or show deviations between theory and measurement outright after comparing the simulated events to experimental data. One of those event generation tools is `SHERPA`. Along with MC event generation in general, it is discussed in more detail in section 3.2.

3.1 The ATLAS Detector

ATLAS (**A** **T**oroidal **L**HC **A**pparatu**S**), as the name suggests, is a cylindrical, toroidal detector with multiple layers that serve different detection purposes and is discussed in the following sections. The coordinate system used is right-handed with the x-axis pointing towards the collider arc centre, and the z-axis along the tunnel. The full coordinate system is illustrated in fig. 3.1. A more detailed

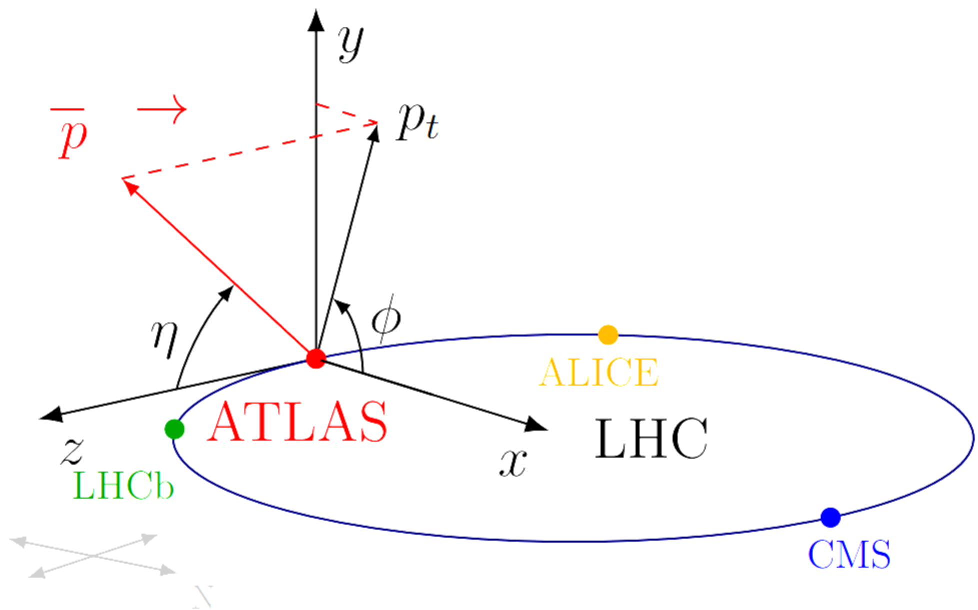

Figure 3.1: The ATLAS coordinate system, from [20]

introduction to the inner workings of the detector, that this introduction is also derived from, can be found in [21, 22].

3.1.1 Inner detector

The innermost layer of the ATLAS detector enables the reconstruction of particle tracks and vertices. It is immersed in a magnetic field of 2 T strength. Charged particles are diverted on circular arcs by the Lorentz force which allows different particle tracks to be recorded by the use of different detectors. Pixel detectors lie close to the beam axis and have high granularity and semiconductor trackers on the surrounding layer with segmented strip layers which together are able to measure the radius R from the beam axis and the polar angle ϕ of the outgoing particles up to a rapidity $|\eta| = 2.5$. In May 2014 the latest large modification of the inner layer was completed. The added insertable B-layer is an innermost pixel detector just 3.3 cm away from the beam axis.

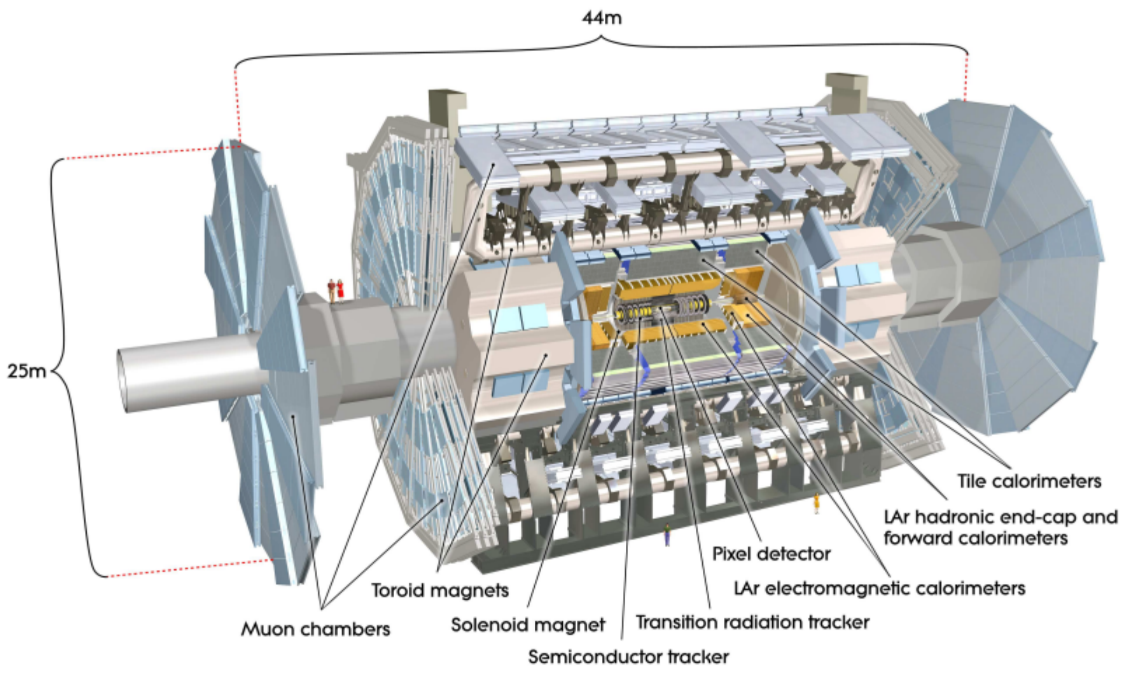

Figure 3.2: The ATLAS detector, from [21]

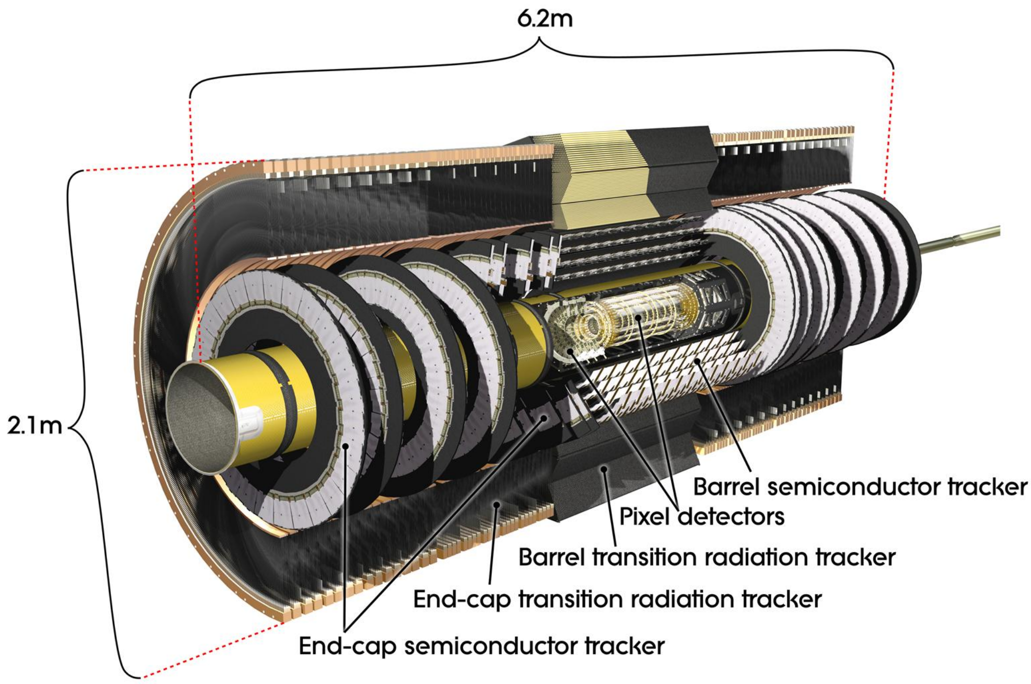

Figure 3.3: The inner detector, from [21]

3.1.2 Calorimeter System

The particle identification and energy measurement is mainly done in the calorimeter system. The basic measurement principle of the calorimeter system are cascade like particle productions in showers. In the EM calorimeter this happens through repeated bremsstrahlung induced photon emissions through electrons and positrons, and photon induced electron-positron pair productions. In the hadronic calorimeter a similar cascade it started through inelastic scattering of hadrons with heavy nuclei which again produces hadrons fueling a chain reaction until the disposed energy is below the pion production thresh hold. These two components must provide good containment of the EM and hadronic showers, insuring that the particles dispose all their energy in the calorimeter and limiting punch through into the muon system. The full assembly is housed in different cryostats.
The EM calorimeter is highly granulated, making it ideal for precise measurements of electrons and photons. It includes a barrel portion that spans up to $|\eta| = 1.475$, as well as two end caps on each side of the detector, spanning from $1.375 < |\eta| < 3.2$. The EM calorimeter is composed of lead-liquid argon (lead-LAr) detectors, with kapton electrodes that are accordion-shaped and lead absorber plates that span its complete area.
The tile calorimeter is situated directly outside the EM calorimeter envelope and encompasses the region up to $|\eta| = 1.0$ using steel absorbers and scintillating tiles as the active medium for its barrel. Its two extended barrels cover the range of $0.8 < |\eta| < 1.7$. The Hadronic End-cap Calorimeter (HEC) includes two independent wheels per end-cap located just behind the end-cap EM calorimeter. Each wheel contains 32 identical wedge-shaped modules and is divided into two segments in depth, resulting in four layers per end-cap in total. The Forward Calorimeter (FCal) is integrated into the end-cap cryostats since it provides uniform calorimetric coverage and reduces radiation background levels in the muon spectrometer. It has a depth of approximately 10 interaction lengths and includes three modules in each end-cap. The first module, made of copper, is designed for electromagnetic measurements, while the other two, made of tungsten, are primarily used to measure the energy of hadronic interactions.

3.1.3 Muon Chamber

Because of their comparatively higher mass with regards to the electron, muons do not typically shower within the electromagnetic calorimeter and have to be

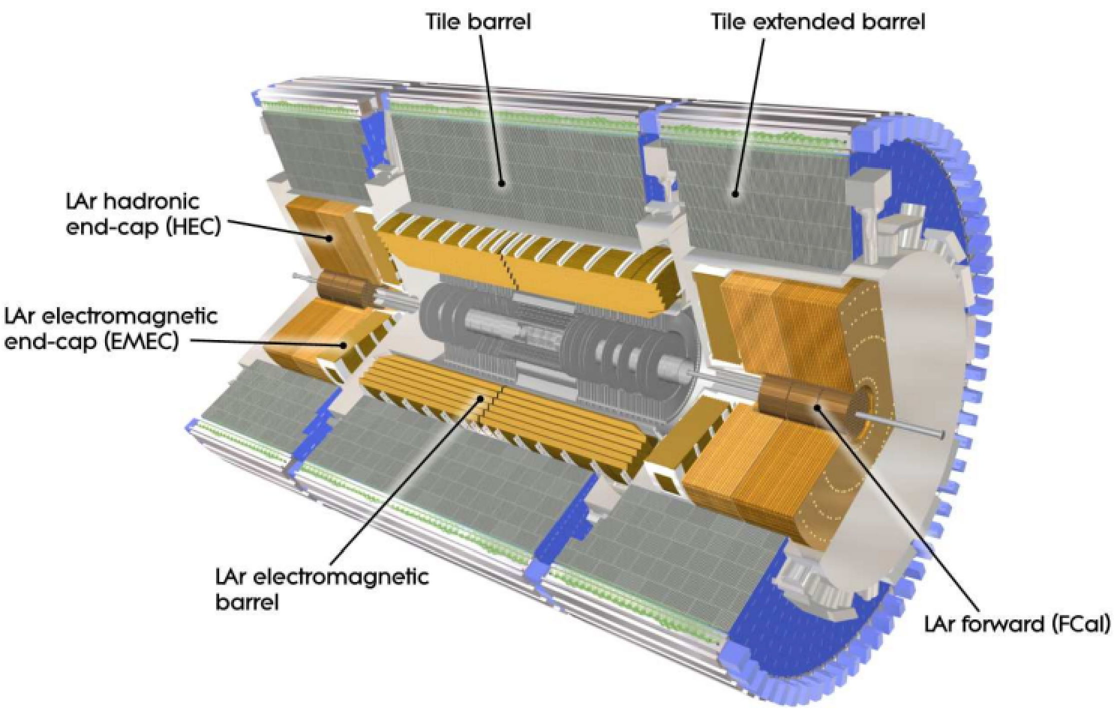

Figure 3.4: The calorimeter system, from [21]

detected separately in its own detector chamber. The muon chamber is based upon the magnetic deflection of muons through both superconducting air-core barrel toroid magnets and end-cap magnets in a tracking chamber. It is wrapped around the calorimeter system and is able to detect muons up to a rapidity $|\eta| = 2.7$. Muons are generally not stopped during the measurement making it the only SM particle to leave the detector next to the undetected neutrinos.

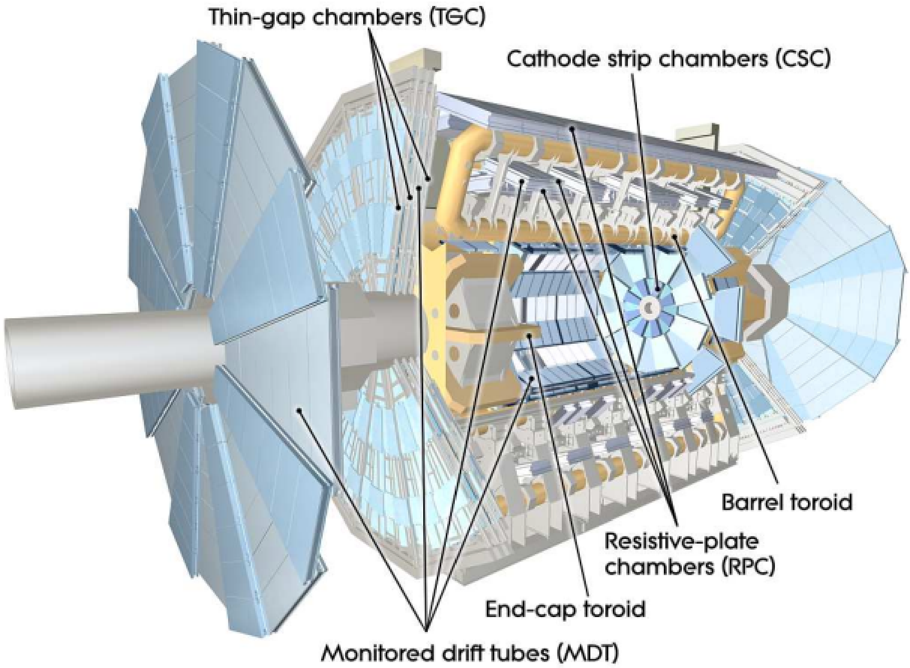

Figure 3.5: The calorimeter system, from [21]

3.2 Monte-Carlo Event Generation and `SHERPA`

Monte Carlo (MC) event generation has become a quintessential tool in development and interpretation of high-energy scattering experiments. Given the enormous amounts of possibly interesting final states and connected physical properties predicted by the SM, detailed analyses have to be done to evaluate both theoretical aspects, like for example predicted differential cross sections, as well as aspects of implementation like calibration of reconstruction algorithms of the experiment. The event generation is based upon (pseudo) random numbers which are used to simulate scattering events following a set of cross sections. This is determined by a set of Feynman rules given by the SM or different theories through a set Lagrangian and is calculated by the use of a numerical phase space integrator. There exist many different MC event generators that are able to simulate different processes of the SM. A very versatile generator is `SHERPA` (**S**imulation of **H**igh-**E**nergy **R**eactions of **PA**rticles) [23]. It is able to cover all reactions of the SM and additional models like SMEFT can be implemented using the Universal FeynRules Output (UFO). The `SMEFTsim_topU3l_MwScheme` UFO model [24] was used to implement the SMEFT operators covered in this thesis. A comprehensive introduction to `SHERPA` can be found in its manual [25].

4 Simulation and Analysis

All event simulations are set up in run cards in the `.yaml` file format that specifies the setup of the event generator ranging from detector energies over particle selectors to the setting of the activation of parton showering. After generating the MC events on the HPC cluster TAURUS [26] they were run through a `C++` analysis within `RIVET` [27], which analyzed the event output regarding physical observables, applied cuts for phase spaces of interest and filled the histograms. Those were plotted within `RIVET` and analyzed further with fitting tools and scaled to luminosities using `Python`. The following chapter will present and discuss the chosen setups and their associated caveats for the SM as well as the SMEFT simulation.

4.1 Event Generation Setup

For all the following event generations `SHERPA version 3.0.0` [28, 23, 25] was used with the LHC-ATLAS beam setup, which means

$$\texttt{BEAMS}: \; 2212 \tag{4.1}$$

for a proton-proton collision and

$$\texttt{BEAM\_ENERGIES}: 6500 \tag{4.2}$$

for beam energies of 6.5 TeV per beam, resulting in a centre of mass energy ($\mathrm{E_{CMS}}$) of 13 TeV. `SHERPA` uses two matrix element generators, `COMIX` and `AMEGIC`. In this thesis both were used for the SM simulation and `COMIX` was used for the SMEFT simulation. The used parton density function was `PDF4LHC21_40_pdfas` and default renormalization, factorization and core scales were used. Multiple generation level cuts were applied which can be found in Table 4.1. An additional split was applied with the transverse momentum of the electron-positron pair in two separate run cards. The reasoning behind this step will be discussed in Section 4.1.1.

Observable	Cut	Comment
$p_{T,\text{Leptons}}$	≥ 5 GeV	All leptons have a minimum transverse momentum
$m_{\text{Lepton Antilepton}}$	≥ 4 GeV	The resulting lepton antilepton pair has a minimum invariant mass

Table 4.1: Generation level cuts. The upper bound is always E_{CMS}.

The mass cut combined with the $p_{T,\text{Z}}$ cut discussed in Section 4.3 helps to reduce the effect of background processes in which a photon γ instead of the Z boson produces the final state leptons.

4.1.1 $\mathbf{pT_Z}$ Split

Figure 4.1 shows that simulating events at event numbers of 10^6 following only the setup discussed in Table 4.1 leads to kinematic variables that have high uncertainties in the high energy regions. To avoid generating a very high amount of events to acquire the necessary low statistical MC uncertainty in the tail ends, the aforementioned split was introduced to break up the event generation into two parts - events with transverse Z momentum $p_{T,Z}$ below and above 150 GeV. Explicitly this was done through generation level cuts following either

$$5 \text{ GeV} \leq \; p_T(e^-, e^+) \; \leq 150 \text{ GeV} \tag{4.3}$$

or

$$150 \text{ GeV} \leq \; p_T(e^-, e^+) \; \leq \text{E}_{\text{CMS}}. \tag{4.4}$$

In both cases the same number of events were generated and analysed. Afterwards they were stack on top of each other to acquire a significantly lower statistical uncertainties in the higher-energy regions.
To be able to implement this, a specific hard process had to be chosen to differentiate the Z boson decay induced leptons from the $W^\pm$ boson decay induced lepton. The decision fell on

$$\texttt{93 93 -> 11 -11 13 -14} \tag{4.5}$$

$$\texttt{Order: \{QCD: 0, EW: 4\},} \tag{4.6}$$

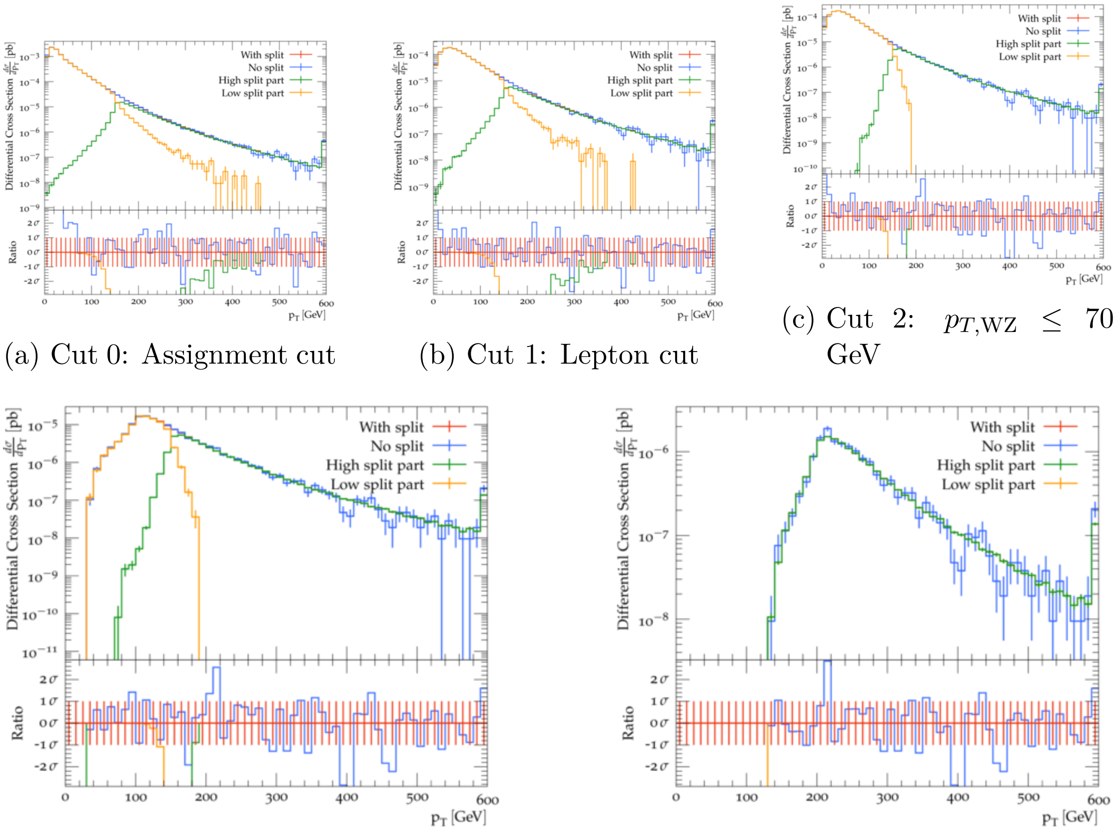

(a) Cut 0: Assignment cut

(b) Cut 1: Lepton cut

(c) Cut 2: $p_{T,\mathrm{WZ}} \leq 70$ GeV

(d) Cut 3: $p_{T,\mathrm{Z}} \geq 100$ GeV

(e) Cut 3: $p_{T,\mathrm{Z}} \geq 200$ GeV

Figure 4.1: Plots for the verification of the consistency of the $p_{T,\mathrm{Z}}$ split. The observable shown is the transverse momentum $p_{T,\mathrm{W}}$ over the five cuts applied. The SM simulation without any Split has noticeably higher uncertainties in the energy tail then the SM simulation with split.

translating to the process

$$\mathrm{p} + \mathrm{p} \longrightarrow \mathrm{e}^- + \mathrm{e}^+ + \mu^- + \nu_\mu \tag{4.7}$$

with two protons in the initial state and an electron positron pair from the Z boson and a muon-muon neutrino pair resulting from the $W^\pm$ decay, while allowing only two vertices as expected on tree level (see Figure 2.1) through the `Order` parameters.

It was verified that this approach resulted in sensible and consistent results by plotting both the fully simulated SM and the SM simulated with the $p_{T,Z}$ split in Figure 4.1.

4.2 EFT Setup

In order to include another model on top of the SM in `SHERPA`, it is necessary to load a Universal Feynman Output (UFO) model that implements the BSM physics and in this case reparameterizes existing couplings and adds new vertices. In this thesis the UFO model `SMEFTsim_topU3l_MwScheme` from [24, 29, 30] is used with `topU3l` denoting a $U(2)^3$ flavour symmetry in the quark sector and a $U(3)^2$ flavour symmetry in the lepton sector as recommended by [31]. The `MwScheme` was used, basing the calculations o n the input parameters m_W, m_Z, G_F.
The chosen nonzero values for the setup parameters in the `UFO_PARAMS` block of the run card can be found in Table 4.2.

Table 4.2: Block Inputs for the SMEFT Model. All other parameters are set to 0.

Block	Parameter	Value
SMEFT Cutoff	Λ	1000 GeV
Yukawa Couplings	y_{mb}	4.18 GeV
	y_{mt}	172.76 GeV
mass	m_Z	91.1876 GeV
	m_t	172.76GeV
	m_b	4.18 GeV
	m_H	125.09 GeV
SMEFT Inputs	m_W	80.387 GeV
	G_f	1.1663787 10^{-5} GeV^{-2}
	α_S	0.1179 GeV

4.2.1 Chosen Operators

All theoretically contributing operators discussed in Section 2.2.1 were input individually into a separate run card and simulated with the SM. As suggested in Ref. [18], which employed the event generator `MadGraph` to arrive at the results, only a subset of the possible operators have nonzero cross section contributions to the process. However, comparisons with the simulation in `SHERPA` showed partially different results: The operators C_{uW}, C_{dW}, $C_{\varphi ud}$, C_{uB}, C_{dB}, C_{eW}, C_{eB}, $C_{\varphi WB}$ and $C_{\varphi \tilde{W}B}$ lead to the error `No Hard Process found` in the integration. This was assumed to be the result of no finite contribution to the cross section. Comparing with the source code of the UFO model implementation, one possible reason for this could be the set Yukawa couplings and masses. Because of negligible values compared to the beam energies, they are set to zero which means that terms

in Feynman rules they contribute to vanish. The $C_{\varphi u}$ and $C_{\varphi d}$ operators caused an infinite loop with the code "`Amplitude::GaugeTest(): zero result. Redo gauge test.`" outright so that integration could not advance. Further investigations into the reason behind the missing hard process showed that more operators produce the aforementioned error if the Yukawa couplings present in the Feynman rule contributions of the affected operators are set to a nonzero value. The issue was noted in a solution has been proposed [32]. Because of the chiral coupling structure of the operators with respect to the incoming partons also resulted in no possible hard process.
Since no simulation with these Operators was possible, they were disregarded for this thesis leaving only the following eight operators for further investigations:

1. $\mathcal{O}_{\varphi \mathrm{D}}$
2. $\mathcal{O}_{\varphi \mathrm{e}}$
3. $\mathcal{O}_{\varphi \mathrm{l1}}$
4. $\mathcal{O}_{\varphi \mathrm{l3}}$
5. $\mathcal{O}_{\varphi \mathrm{q1}}$
6. $\mathcal{O}_{\varphi \mathrm{q3}}$
7. $\mathcal{O}_{\mathrm{W}}$
8. $\mathcal{O}_{\tilde{\mathrm{W}}}$

4.2.2 EFT Orders

The number of different inserted SM and SMEFT vertices in contributing Feynman diagrams is determined by different order parameters. In order to differentiate between the linear interference contributions, resulting from the interference of SM and a SMEFT diagrams, and quadratic pure new physics (NP) contributions, stemming from the SMEFT diagrams alone, one needs to set up the SM and SMEFT interaction orders correctly. After the process definition there are two possible settings of interest, namely the `Order` and the `Max_Amplitude_Order` setting. Both of them take a number of parameters regarding the possible interaction vertices following from the different fundamental interactions.
The `Max_Amplitude_Order` parameter describes the number of vertex insertions on matrix level. `{QCD: 0, QED: Any}`, for example, allows no QCD but any number of EW vertices at tree level for the given process. `NP: x, NPcO: x` allows for x insertions of a vertex given by the SMEFT operator $\mathcal{O}$ with coefficient `cO` on matrix element level.
The `Order` parameter sets the interaction order according to the squared modulus of the matrix element (cross section level). This is best understood with an example: Given a Feynman diagram with one electroweak and one NP insertion as seen in Figure 4.2, the SM vertex counts as g_{SM} on matrix element and $\alpha_{SM} = g_{SM}^2$ on cross section level. The NP vertex insertion counts as $g_{NP} g_{SM}^2$ on

matrix element and $\alpha_{NP}\alpha_{SM}^2 = g_{NP}^2 g_{SM}^4$ on cross section level. Since the idea behind the SMEFT NP vertex was originally an integrated out propagator, two SM vertices are "hidden" inside the NP vertex and have to be included in the counting. The full diagram then leads to a cross section level squared matrix element like

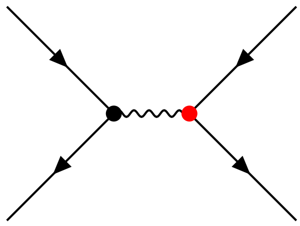

Figure 4.2: Example diagram with the SM vertex insertion in black and the NP vertex insertion in red

the one already seen in Equation (2.22) with the corresponding cross section in Equation (2.23) with corresponding coupling orders

$$|\mathcal{M}_{SM}|^2 \propto g_{SM}^2 = \alpha_{SM} \tag{4.8}$$
$$|\mathcal{M}_{SM}\mathcal{M}_{NP}| \propto g_{SM}^3 g_{NP} = \alpha_{SM}^{1.5}\alpha_{NP}^{0.5} \tag{4.9}$$
$$|\mathcal{M}_{NP}|^2 \propto g_{SM}^4 g_{NP}^2 = \alpha_{SM}^2 \alpha_{NP} \tag{4.10}$$

By specifying both the `Order` and the `Max_Amplitude_Order` it is possible to extract only the linear or quadratic SMEFT contribution of a given operator. This method of decomposition of the linear interference contribution and quadratic pure SMEFT contribution is similar to the one used in [33]. A corresponding setup for the linear case would be

```
Max_Amplitude_Order:{QCD: 0, QED: Any, SMHLOOP: 0, NP: 1, NPcO: 1}
```
(4.11)

```
Order:{QCD: 0, QED: Any, SMHLOOP: 0, NP: 0.5, NPcO: 0.5}
```
(4.12)

and for the quadratic case

```
Max_Amplitude_Order:{QCD: 0, QED: Any, SMHLOOP: 0, NP: 1, NPcO: 1}
```
(4.13)

```
Order:{QCD: 0, QED: Any, SMHLOOP: 0, NP: 1, NPcO: 1}
```
(4.14)

allowing any number of EW vertices, no QCD vertices and only one NP insertion at any point in the process. Another approach that could be taken is simulate the full SM and SMEFT contribution together and extracting the linear and quadratic terms in a way discussed in Section 4.3.2.
With the discussed setup, simulations were done for both the SM as well as the SMEFT operators. One million unweighted showered events were generated for each of the $p_{T,Z}$ splits of the SM and all sixteen operator contributions adding up to two million events for the SM and four million for each of the eight operators. For the Wilson coefficients of the operators a value of $c_O = 10$ was set up for all operators to be able to see possible deviations in the phase space which might not be visible at current bounds. Scaling down to the desired Wilson coefficient for later comparisons should be more reliable then scaling up from it to a more visible coefficient. A similar approach regarding the scaling of coefficients was taken in [33]. The rescaling to the desired Wilson coefficients is discussed in Section 4.3.1

4.3 Rivet Analysis

After the event generation, all events were analysed by `RIVET` using a preexisting analysis taken from Ref. [34] in which different successively more restrictive cuts are applied and all histograms used in further data evaluation are filled with the events after the respective cuts. The applied cuts can be found in Table 4.3. The analysed samples are plotted utilizing the `rivet-cmphistos` and `make-plots` scripts with respect to multiple different observables listed below.

- Transverse momenta of the
  - $W^{\pm}Z$ system: $p_{T,\mathrm{WZ}}$
  - $W^{\pm}$ boson: $p_{T,\mathrm{W}}$
  - Z boson: $p_{T,\mathrm{Z}}$
  - Charged lepton coming from the $W^{\pm}$ boson: $p_{T,\mathrm{W\ lepton}}$
- Invariant mass of the
  - $W^{\pm}Z$ system m_{WZ}
  - Z boson: m_{Z}
  - All resulting Leptons: m_{Leptons}
  - Transverse mass of the $W^{\pm}Z$ system: $m_{T,\mathrm{WZ}}$

- Transverse mass of the $W^{\pm}$ boson: $m_{T,\mathrm{W}}$

- $R_{21} = \min\left(\frac{p_W}{p_Z},\ \frac{p_Z}{p_W}\right)$: Ratio of $W^{\pm}$ and Z boson momenta
- p_{MET}: Missing transverse momentum
- Pseudorapidity difference
  - $\Delta\eta_{\mathrm{W,\,Z}}$: Difference between $W^{\pm}$ boson and Z boson pseudorapidity
  - $\Delta\eta_{\mathrm{W\ lepton,\,Z}}$: Difference between charged W lepton and Z pseudorapidity
  - $\Delta\eta_{\mathrm{W\ lepton,\,Z\ leptons}}$: Difference between charged W lepton and Z leading lepton pseudorapidity
- $y_{\mathrm{W\ lepton}}$: Rapidity of the charged $W^{\pm}$ lepton
- Scattering angle
  - of $W^{\pm}$ boson with respect to the beam axis
    * in the lab frame: $\cos\theta_W^{\textbf{lab frame}}$
    * in the $W^{\pm}Z$ boson pair centre of mass frame: $\cos\theta_W^{\textbf{WZ frame}}$
  - of Z boson with respect to the beam axis
    * in the lab frame: $\cos\theta_Z^{\textbf{lab frame}}$
    * in the $W^{\pm}Z$ boson pair centre of mass frame: $\cos\theta_Z^{\textbf{WZ frame}}$
  - of the charged W lepton
    * in the $W^{\pm}$ boson rest frame with respect to the $W^{\pm}$ boson momentum in the lab frame: $\cos\theta_{W\ \mathrm{Lep}}^{\textbf{W lab}}$
    * in the frame boosted first in to the $W^{\pm}Z$ centre of mass frame then $W^{\pm}$ rest frame with respect to the $W^{\pm}$ boson momentum in the $W^{\pm}Z$ centre of mass frame: $\cos\theta_{W\ \mathrm{Lep}}^{\textbf{WZ into W}}$
  - of the negatively charged Z lepton
    * in the Z frame with respect to the Z in the $W^{\pm}Z$ frame: $\cos\theta_{Z\ \mathrm{Lep}}^{\textbf{Z lab frame}}$
    * in the a frame boosted first in to the $W^{\pm}Z$ then Z frame with respect to the Z boson in the $W^{\pm}Z$ frame: $\cos\theta_{Z\ \mathrm{Lep}}^{\textbf{WZ into Z frame}}$
- $\Delta\phi_{\mathrm{W\ lepton,\,Z\ lepton}}^{\textbf{Lab}}$: Azimuthal angle difference between negatively charged Z lepton and charged $W^{\pm}$ lepton with both being in the lab frame

- $\Delta\phi^{\textbf{WZ frame}}_{\text{W lepton, Z lepton}}$: Azimuthal angle difference between the negatively charged Z lepton and the charged W lepton in the $W^{\pm}Z$ frame

Table 4.3: Applied Cuts in the `RIVET` analysis

Cut 0:	Selection cut	# charged leptons = 3 # neutrinos = 1
Cut 1:	Lepton cut	$p_{\text{T, W lepton}} > 20$ GeV $p_{\text{T, Z lepton}} > 15$ GeV $\lvert\eta_{\text{lepton}}\rvert < 2.5$ $m_{T,W} > 30$ GeV Δy(Z leptons) > 0.2 Δy(Z lepton and W lepton) > 0.3
Cut 2:	WZ system	$p_{\text{T, WZ}} < 70$ GeV
Cut 3:	Transverse Z momentum	$p_{\text{T, Z}} > 100$ GeV or $p_{\text{T, Z}} > 200$ GeV

4.3.1 Contribution Merging

After simulating the contributions separately in the way discussed in Section 4.2.2 and running them through the `RIVET` analysis the contributions are combined to acquire the full simulation of the SM with the SMEFT operators as introduced in Equation (2.23). To do this the histogram files in the `.yoda` file format were stacked on top of each other using `yodastack` from the `YODA` data analysis tool [35]. The scaling to the appropriate Wilson coefficients was performed in the same step by multiplying the linear contributions with $\frac{c_W}{10}$ and the quadratic contributions with $\frac{c_W^2}{100}$. The division by 10 was done to remove the previous simulation coefficient of 10 as noted in Section 4.2.2. The Wilson coefficients are chosen to be in line with current experimental bounds and are presented in Table 4.4.

4.3.2 Interference Factor and Closure

Multiple tests were done to verify the consistency of the decomposition approach. As previously discussed, the linear and quadratic contributions of the SMEFT operators were simulated separately by specifying the order parameters as discussed in Section 4.2.2. By simulating the SM with additional SMEFT operators up to and including quadratic SMEFT order with both positive $\mathcal{M}(c)$ as well as negative $\mathcal{M}(-c)$ Wilson coefficients of the same absolute value and combining both, so that

Table 4.4: Bounds of all simulated operators. The lowest bound was selected from all considered sources if multiple bounds existed.

Operator	negative	positive
$\mathcal{O}_{\varphi D}$	-2.5 [36]	1.1 [36]
$\mathcal{O}_{\varphi e}$	-0.41 [37]	0.79 [37]
$\mathcal{O}_{\varphi l1}$	-0.23 [36]	0.098 [36]
$\mathcal{O}_{\varphi l3}$	-0.29 [36]	0.1 [36]
$\mathcal{O}_{\varphi q1}$	-0.11 [36]	0.33 [36]
$\mathcal{O}_{\varphi q3}$	-0.14 [38]	0.11 [36]
$\mathcal{O}_{W}$	-0.15 [36]	0.04 [38]
$\mathcal{O}_{\tilde{W}}$	-0.17 [36]	0.18 [36]

with Equation (2.23) the contributions can be calculated as

$$\frac{1}{2}\left(|\mathcal{M}(c)|^2 - |\mathcal{M}(-c)|^2\right) = 2c\,|\mathcal{M}_{SM}\mathcal{M}_{NP}| \tag{4.15}$$

$$\frac{1}{2}\left(|\mathcal{M}(c)|^2 + |\mathcal{M}(-c)|^2\right) = c^2\,|\mathcal{M}_{NP}|^2 \tag{4.16}$$

This makes it possible to extract the contributions by the means of a full and not by a separate simulation. Now a comparison between the two approaches of either decomposing the simulation into linear and quadratic contributions or simulating SM and SMEFT contributions in full and extracting the contributions afterwards can be done to verify the validity of the decomposition method used further on in the thesis. In theory these approaches should show the same results if the integration and generation behaves the same way. At first it had to be tested whether the factor of two, that arises in the linear term of the quadratic binomial expansion of the matrix element in Equation (2.22), is already included in the simulated linear contribution or has to be added during the contribution merging. The use of Equation (4.15) makes this possible. Plotting the results in Figure 4.4 shows that the linear factor is already contained in the separately simulated linear term. It has to be noted that some observables like Figure 4.3 still show deviations especially at lower cuts which leads to the second test, which focuses on the quadratic contribution.

Some observables show differences between the two contribution approaches not only at linear order. Especially at quadratic order like in Figure 4.5a, which was calculated following Equation (4.16), large deviations appear. Investigations into this, comparing integration and generation level cross sections between the two contribution calculations in Table 4.5 showed significant differences at both levels.

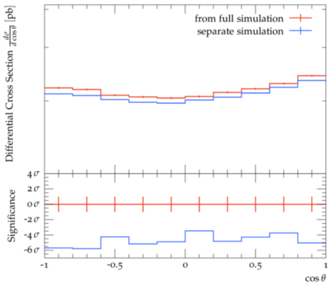

(a) Cut 0: Assignment cut

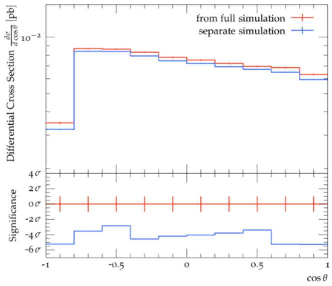

(b) Cut 1: Lepton cut

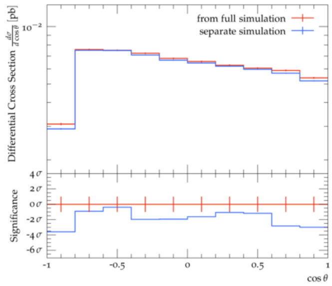

(c) Cut 2: $p_{T,\text{WZ}} \leq 70$ GeV

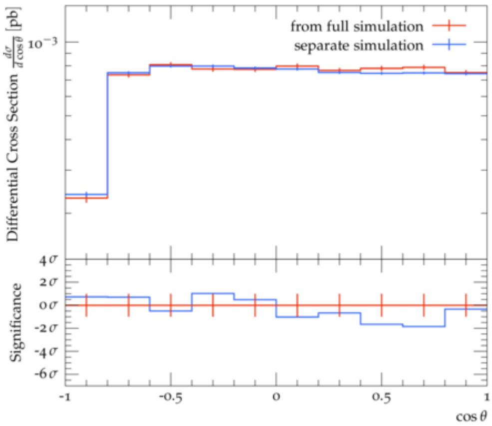

(d) Cut 3: $p_{T,\text{Z}} \geq 100$ GeV

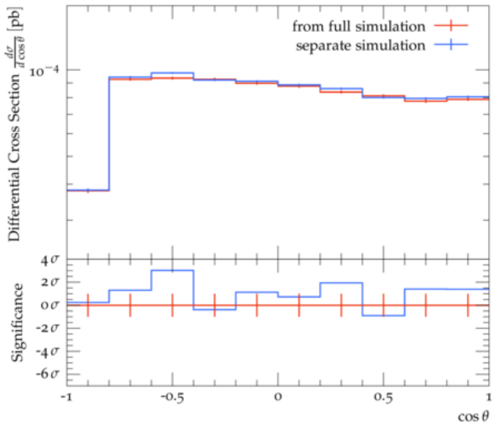

(e) Cut 3: $p_{T,\text{Z}} \geq 200$ GeV

Figure 4.3: Plots for the verification of the factor 2 in the linear contribution in the SMEFT simulation. The observable shown is the scattering angle of the lepton coming from the $W^{\pm}$ boson in the $W^{\pm}$ boson rest frame $\cos\theta_{\text{W lepton}^{\textbf{W rest frame}}}$ over the five cuts applied.

Further studies revealed that the simulation included scattering contributions in

Table 4.5: Integration and generation cross sections for single and full simulated contributions as well as their respective ratios $\frac{\text{Full}}{\text{Separate}}$

	integration	generation
Full simulation linear:	(-0.0431 ± 0.0004) pb	(-0.0436 ± 0.0004) pb
Linear separate:	(-0.0436 ± 0.0004) pb	(-0.0419 ± 0.0004) pb
Linear ratio:	0.988 ± 0.014	1.040 ± 0.015
Full simulation quadratic:	(0.0256 ± 0.0003) pb	(0.0253 ± 0.0003) pb
Quadratic separate:	(0.0291 ± 0.0003) pb	(0.0281 ± 0.0003) pb
Quadratic ratio:	0.881 ± 0.012	0.901 ± 0.013

which the Z boson was replaced by a γ which is massless. It therefore resonates

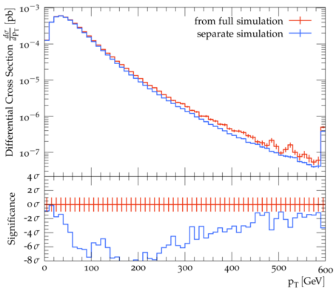

(a) Cut 0: Assignment cut

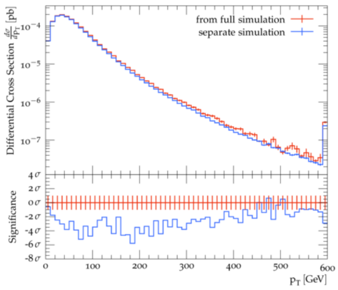

(b) Cut 1: Lepton cut

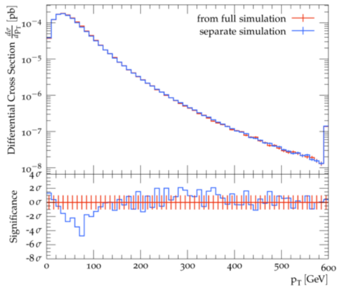

(c) Cut 2: $p_{T,\text{WZ}} \leq 70$ GeV

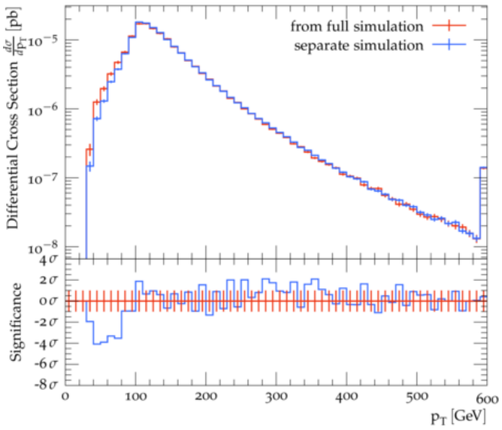

(d) Cut 3: $p_{T,\text{Z}} \geq 100$ GeV

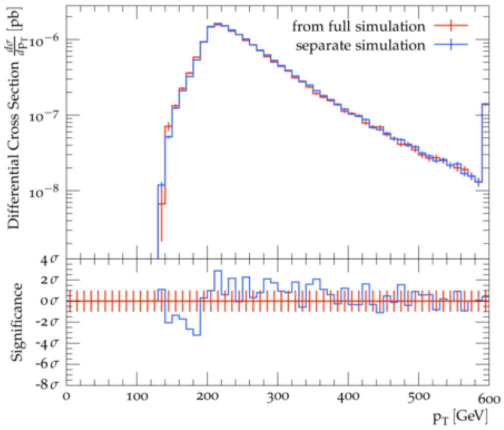

(e) Cut 3: $p_{T,\text{Z}} \geq 200$ GeV

Figure 4.4: Plots for the verification of the factor 2 in the linear contribution in the SMEFT simulation as well as the general closure between the separate linear contribution simulation and the extracted linear contribution from the full simulation as described in Section 4.3.2. The observable shown is the transverse momentum $p_{T,\text{W}}$ over the five cuts applied.

at lower energies and therefore only contributes before the first cut like in Figures 4.6a and 4.6b.

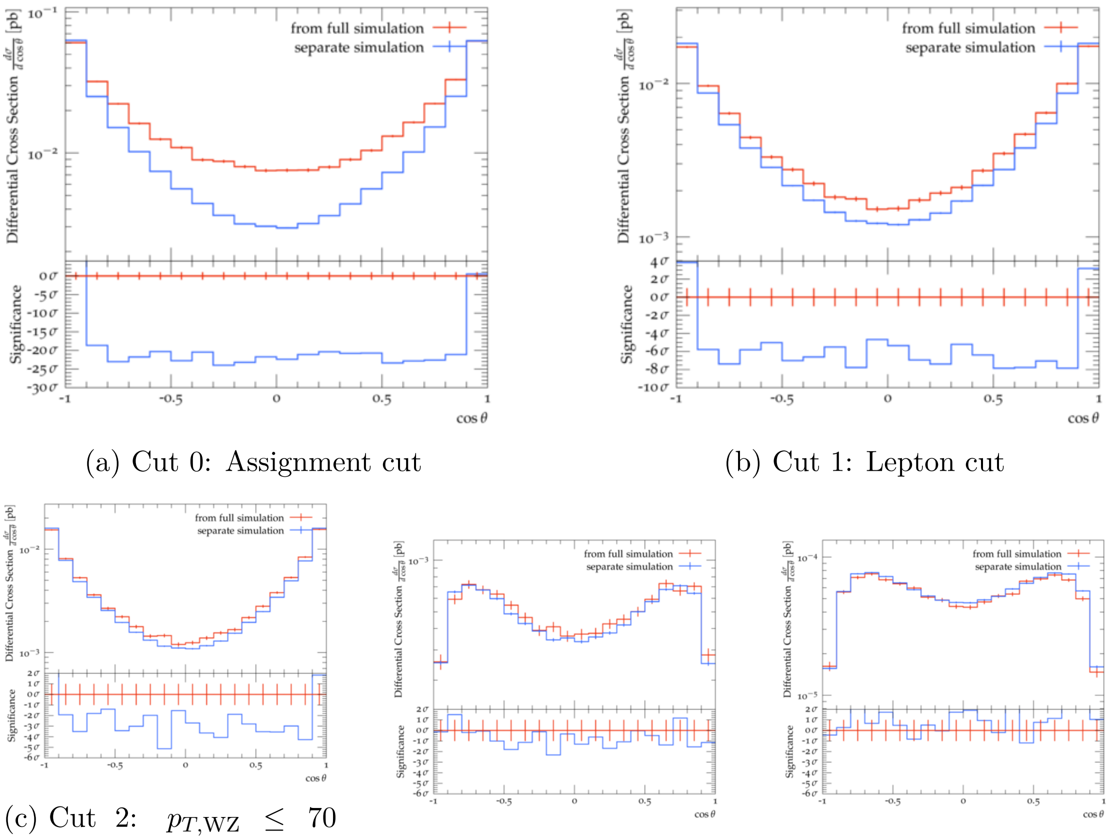

(a) Cut 0: Assignment cut

(b) Cut 1: Lepton cut

(c) Cut 2: $p_{T,\mathrm{WZ}} \leq 70$ GeV

(d) Cut 3: $p_{T,\mathrm{Z}} \geq 100$ GeV

(e) Cut 3: $p_{T,\mathrm{Z}} \geq 200$ GeV

Figure 4.5: Plots for the verification of the closure between the separate quadratic contribution simulation and the extracted quadratic contribution from the full simulation as described in Section 4.3.2. The observable shown is the scattering angle of the $W^{\pm}$ boson in the $W^{\pm}Z$ frame $\cos\theta_{\mathrm{W}}^{\mathbf{WZ\ frame}}$ over the five cuts applied. Especially in cut 0 the deviation surpasses 20σ with deviations lowering at higher cuts.

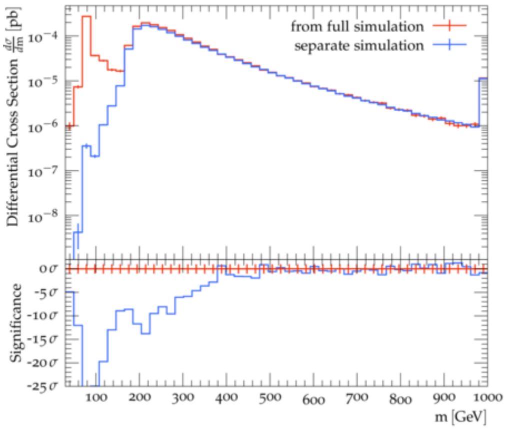

(a) Cut 0: Assignment cut

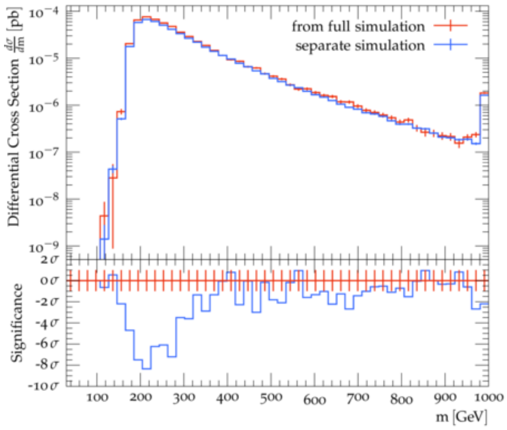

(b) Cut 1: Lepton cut

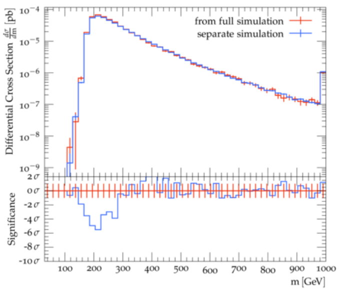

(c) Cut 2: $p_{T,\mathrm{WZ}} \leq 70$ GeV

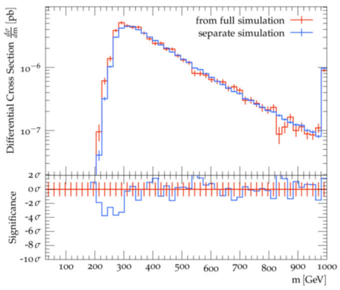

(d) Cut 3: $p_{T,\mathrm{Z}} \geq 100$ GeV

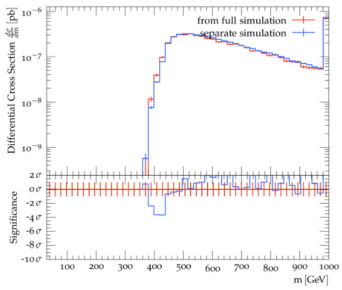

(e) Cut 3: $p_{T,\mathrm{Z}} \geq 200$ GeV

Figure 4.6: Plots for the verification of the closure between the separate quadratic contribution simulation and the extracted quadratic contribution from the full simulation. The observable shown is the mass of the $W^{\pm}Z$ system m_{WZ} over the five cuts applied. In cut 0 two peaks at around 80 GeV and 170 GeV can be seen. The second is assumed to be the (expected) resonance of the combined masses of the $W^{\pm}$ and Z boson at 171 GeV. The first, since it is approximately at the $W^{\pm}$ mass is assumed to be the resonance of the $W^{\pm}$ boson and a second massless particle which might be the photon. At higher cuts only tail events can still be seen resulting in smaller deviations in the left histogram part.

4.4 Sensitivity Observations and Fitting

Only observables based on the measurement of events that passed the third selection cut at $p_{T,Z} = 100$ GeV or $p_{T,Z} = 200$ GeV were considered for the sensitivity study and during the fit. This was done since this hard cut is the one that distinguishes this polarization phase space from comparable ones.

4.4.1 Luminosity Scaling

In order to prepare the data for fitting, the cross section had to be scaled with the luminosity to receive the number of expected events. Before that, additional correction factors had to be applied. At first, only one of four possible flavour combinations ($lll\nu = ee\mu\nu_\mu$) was simulated which results in an additional factor of four since at the energy scales at the LHC the masses of leptons and muons are negligible and all flavour combinations have similar cross sections. Since the data was taken at LO, NLO correction factors have been applied leading to a factor of $\frac{0.7}{0.2} = \underline{3.5}$ [39]. The detector efficiency has also been taken taken into account leading to scaling the simulation by a factor of $\underline{0.5}$ derived from Ref. [40]. The full Run 2 luminosity of the LHC is around 140 fb^{-1}. By multiplying the cross section with the product of these factors, the rescaling to number of expected events is achieved which can be seen in Figures 5.6a and 5.6b. With rebinning like in Figures 5.6c and 5.6d higher significance per bin can be achieved since relative statistical uncertainty per bin $\frac{\Delta N}{N}$ scales with $\frac{1}{\sqrt{N}}$ and therefore decreases with increasing event number N.

4.4.2 Fitting Procedure

The selection of observables used for fitting is based on pointwise significance of the bin entry at current bounds and the contribution's distribution shape. The significance of the bin entry deviations with respect to the SM is calculated by

$$Z = \frac{N_{SMEFT} - N_{SM}}{\Delta N_{SM}}$$

and allows to get a rough estimate on the effectiveness of the fit regarding the setting of new bounds between the possible choices of observables.

The distribution shape can be better seen with the help of the ratio between the full SMEFT simulation and the SM

$$r = \frac{N_{SMEFT}}{N_{SM}}$$

since the shape is not distorted by the uncertainty. For each operator one observable which showed high pointwise significance at the current bounds was chosen to be run through the fitting program. Only the events after the third cut at 100 and 200 GeV are studied. The fitting program takes the SM and the SMEFT contributions as well as their respective MC uncertainties as input and runs through different Wilson coefficients until an upper and a lower limit with the desired significances of 2σ are found. The bin uncertainties are computed by the program itself following Poisson statistics and do not have to be specified beforehand.

5 Results and Conclusion

5.1 Results

5.1.1 Operators

Even though a large number of operators should contribute to the process in theory it was seen that only a subset generates a hard process in `SHERPA`. Investigations into the implementation found that non contributing operators had either Yukawa couplings set to zero resulting in contributions vanishing on the integration level, or `Gauge test` errors occurring that made simulations with these operators impossible. Comparisons with sources which looked at the $W^{\pm}Z$ production process in `MadGraph` [18] showed different contributing operators in some cases. This inconsistency between `SHERPA` and `MadGraph` requires further investigation.

5.1.2 Closure

Currently it is unclear why the separately simulated quadratic contribution is not including the photon resonance. Observables like Figures 4.5b and 4.5c still show significant deviations after the first cut which may not be explained by the additional photon contribution. Understanding the nature of these deviations between the two generation methods is crucial to understanding the EFT implementation into `SHERPA` and needs further investigation beyond this thesis.

5.1.3 EFT Sensitivity

Across all eight studied operators, EFT induced deviations from the SM are visible. For the EFT cross section in Equation (2.23) to be the same as the SM cross section the scaled linear and quadratic terms would need to cancel each other which is not possible for all but the two specific values of the Wilson coefficients in Equation (2.24). Therefore nonzero contributions resulting in nonzero deviations

are expected in all cases.
Equally distributed deviations, which result in flat lines in the ratio plot like in Figure 5.7 that are independent of the observable range are expected, since in many cases the operator's Feynman rule contributions have the same shape as the SM. Therefore the operator only adds to the coupling factor in front of the shape defining terms in the Feynman rule with a strength defined by the Wilson coefficient.
More interesting for the study of this particular phase space are the observables which show a clear shape effect. In these, the deviation changes over the the observable range since in these cases the EFT operator modulates a new shape on top of the existing SM distribution which is easier to spot and more significant to fit.
In all of the following plots the SM is plotted with EFT contribution corresponding to the current positive and negative bound denoted as positive and negative contribution respectively.

$\mathcal{O}_{\varphi D}$:

The $\mathcal{O}_{\varphi D}$ operator shows in Figure 5.4 sensitivity in both the low and high $p_{T,Z}$ cut as well as in the standard and rebinned version with a clear shape effect. A shape effect is also visible in Figure 5.5 even though the significance is low at the chosen luminosity of 140 fb^{-1} in this case. Similar arguments can be made for the $\mathcal{O}_{\varphi q1}$ operator whose plots and discussion can be found in the Appendix A.
The $\mathcal{O}_{\varphi D}$ operator is particularly interesting since the operator only affects propagator mass corrections which with the current understanding according to the SMEFT documentation ([30], Section 6.1) should only work up to linear order $\mathcal{O}(\Lambda^{-2})$. Therefore the $\mathcal{O}_{\varphi D}$ operator, that only affects the Z propagator should not have a quadratic contribution. However, it seems that the quadratic contribution for example in Figure 5.1 is nonzero. This apparent contradiction with respect to the UFO implementation requires further investigations into the origin of these contributions.

$\mathcal{O}_{\varphi e}$:

The $\mathcal{O}_{\varphi e}$ operator shows no shape effect in both Figures 5.6 and 5.7. In both cases the ratio with respect to the SM seems to stay at around 1.1 for the negative and 0.85 for the positive contribution. Similar arguments can be made for the $\mathcal{O}_{\varphi l1}$

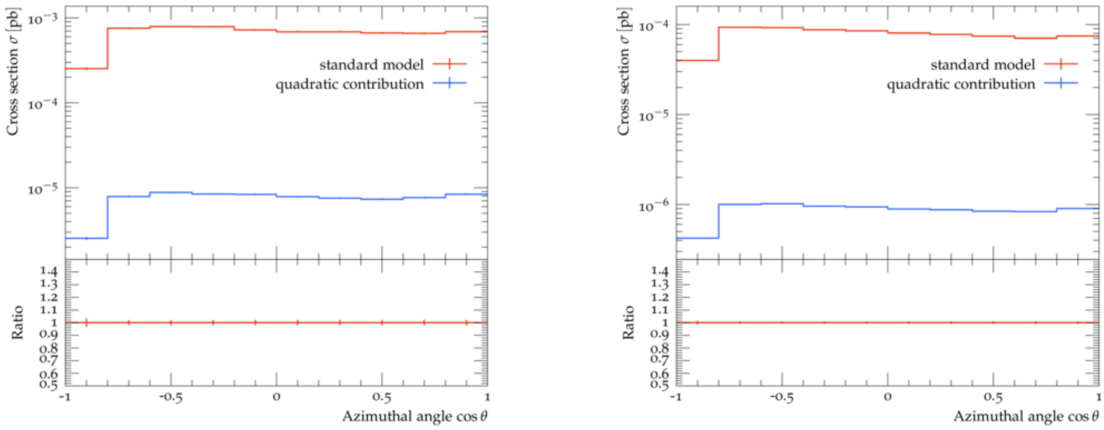

(a) $p_{T,\mathrm{Z}} \geq 100$ GeV, rebinned (b) $p_{T,\mathrm{Z}} \geq 200$ GeV, rebinned

Figure 5.1: The quadratic contribution scaled to the current upper bound of $c = 0.11$ of the $\mathcal{O}_{\varphi D}$ in the $\cos\theta_{W\ \mathrm{Lep}}^{\mathbf{WZ\ into\ W}}$ observable

and $\mathcal{O}_{\varphi l3}$ operators and are discussed in Appendix A.

$\mathcal{O}_{\varphi q3}$:

The $\mathcal{O}_{\varphi q3}$ operator has a high influence in the investigated phase space. As can be seen in Figure 5.8 the deviations are very high in both the high bin and rebinned distributions with pointwise significances of up to 3σ and 8σ for the current bounds. Additionally, the contribution stemming from the negative bound seems to make the cross section negative which would be nonphysical and, if significant, would make it possible to put even tighter constraints on the negative Wilson coefficient for this operator.

$\mathcal{O}_{W}$:

The deviations produced by $\mathcal{O}_W$ are most prominent and significant in the tails of the distribution. Since SMEFT parameterises those high energy deviations as shown in Figure 2.4 it is expected to receive a distribution as shown in Figure 5.9. Interestingly, since in this case both the contributions stemming from the negative and positive bound are positive and have the same shape, the linear contribution is negligibly small compared to the quadratic contribution. Plotting only the individual contributions against each other in Figure 5.2 confirms this. This leads to the conclusion that, unless the Wilson coefficient is four orders of magnitude smaller then the current bounds used in this study and the quadratic contributions is strongly suppressed, the linear contribution can be neglected in further simulations, leaving only the quadratic contribution to be studied. This was already suggested in Section 9.2.7 of Ref. [33].

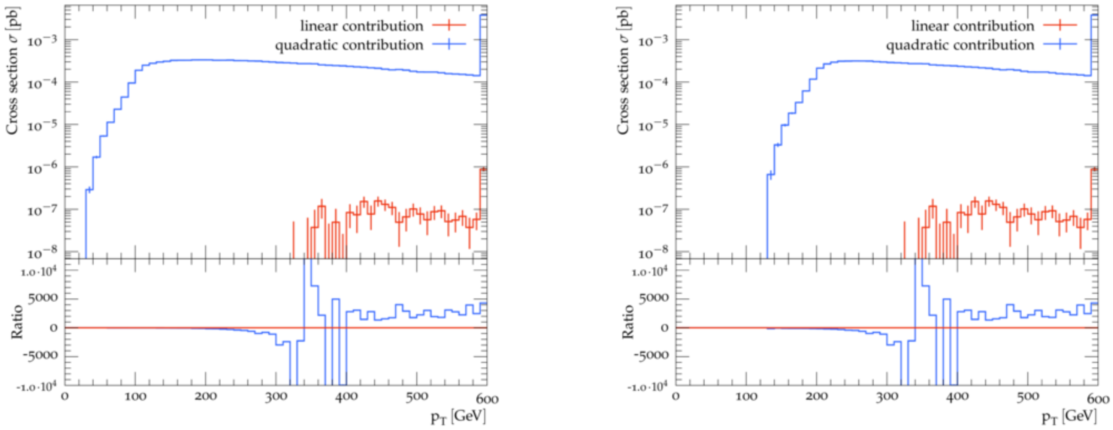

(a) $p_{T,\mathrm{Z}} \geq 100$ GeV, rebinned

(b) $p_{T,\mathrm{Z}} \geq 200$ GeV, rebinned

Figure 5.2: Plots of the linear and quadratic $\mathcal{O}_{\tilde{W}}$ operator contributions of the observable $p_{T,W}$.

$\mathcal{O}_{\tilde{W}}$:

Similarly to $\mathcal{O}_W$, the $\mathcal{O}_{\tilde{W}}$ operator shows significant deviations in the high energy tail in Figure 5.10. Again, the quadratic contribution is two to three orders of magnitude larger than the linear contribution. With similar arguments as before, the linear contribution can be neglected as long as the Wilson coefficient is not decreased by three orders of magnitude.

5.1.4 Fitting

The results for each operator are found in Table 5.1. Even though the scaling to event number was done based on rough estimates of detector effects and NLO corrections, the results show a good estimate as to how sensitive the phase space is to SMEFT effects and whether further investigations into the studied operators is fruitful.

At the current binning only the Wilson coefficients of $\mathcal{O}_{\tilde{W}}$ and $\mathcal{O}_{\varphi q3}$ operators were harder constrained with respect to the old coefficients. The fit at the higher cut value of 200 GeV only had a positive impact in the positive contribution of $\mathcal{O}_W$. However, the fit was done with crude and unoptimized bin sizes and numbers.

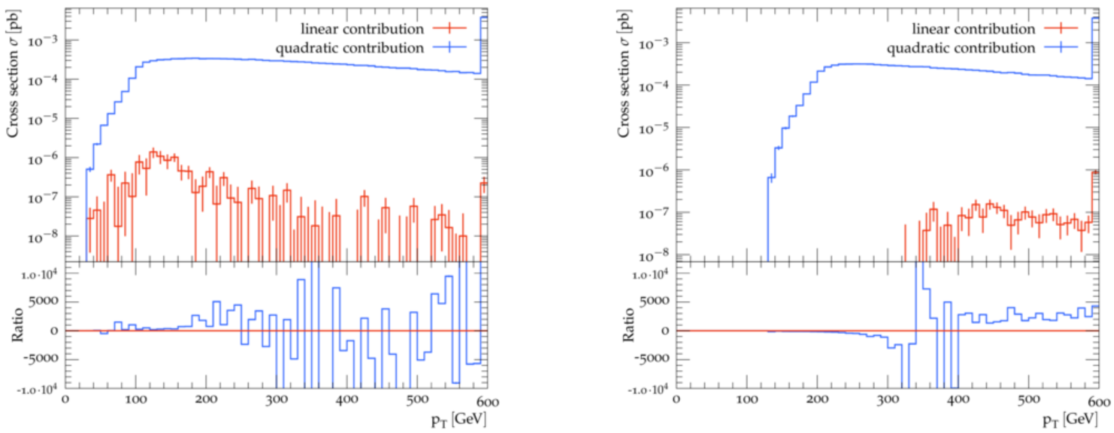

(a) $p_{T,\mathrm{Z}} \geq 100$ GeV, rebinned (b) $p_{T,\mathrm{Z}} \geq 200$ GeV, rebinned

Figure 5.3: Plots of the linear and quadratic $\mathcal{O}_W$ operator contributions of the observable $p_{T,W}$.

Even at this stage many operators which could not be further constrained lie close compared to the old bounds which might make it possible to constrain more operators in this phase space with further bin optimizations.

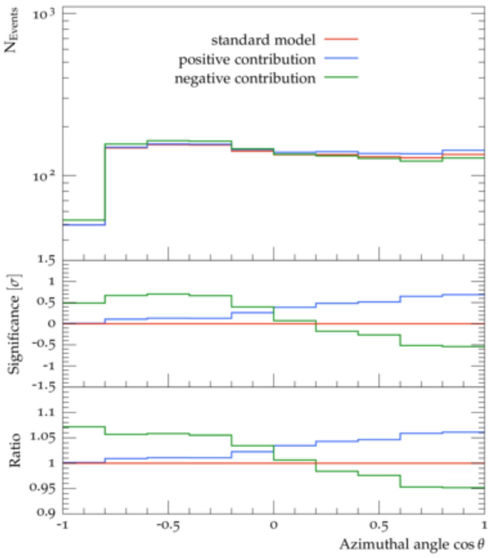

(a) $p_{T,\mathrm{Z}} \geq 100$ GeV

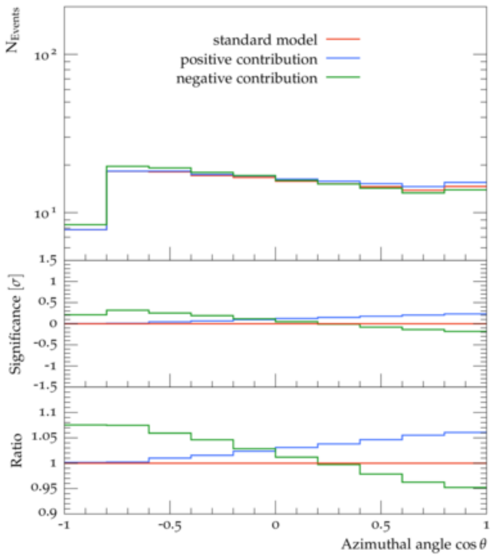

(b) $p_{T,\mathrm{Z}} \geq 200$ GeV

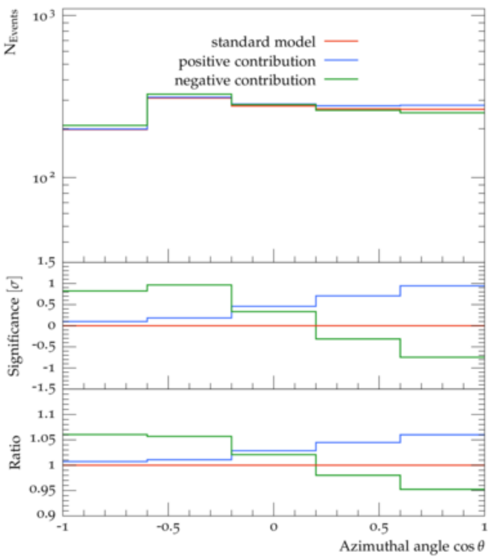

(c) $p_{T,\mathrm{Z}} \geq 100$ GeV, rebinned

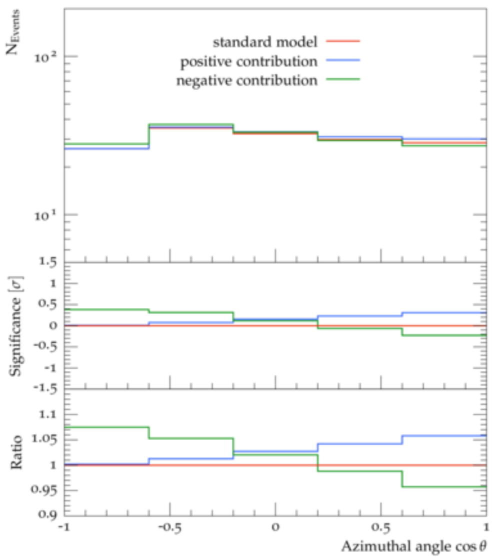

(d) $p_{T,\mathrm{Z}} \geq 200$ GeV, rebinned

Figure 5.4: Plots of the chosen observable for the fit of the $\mathcal{O}_{\varphi D}$ operator. The observable shown $\cos\theta_{W\ \mathrm{Lep}}^{\mathbf{WZ\ into\ W}}$.

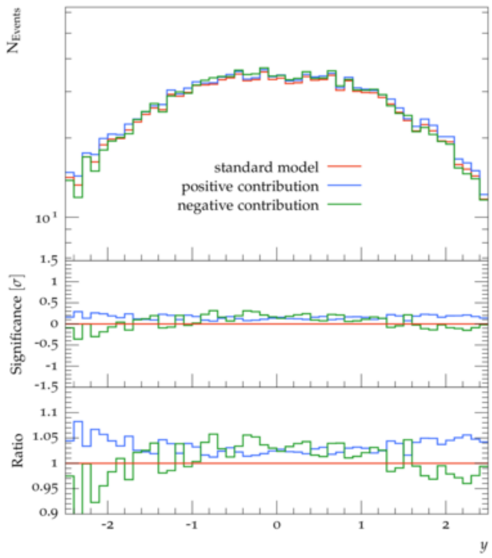

(a) $p_{T,\mathrm{Z}} \geq 100$ GeV

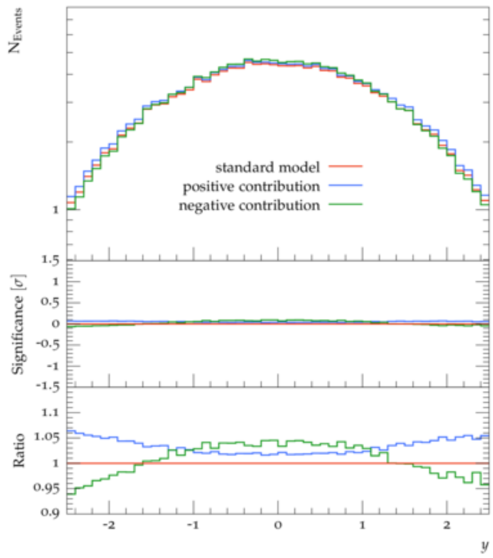

(b) $p_{T,\mathrm{Z}} \geq 200$ GeV

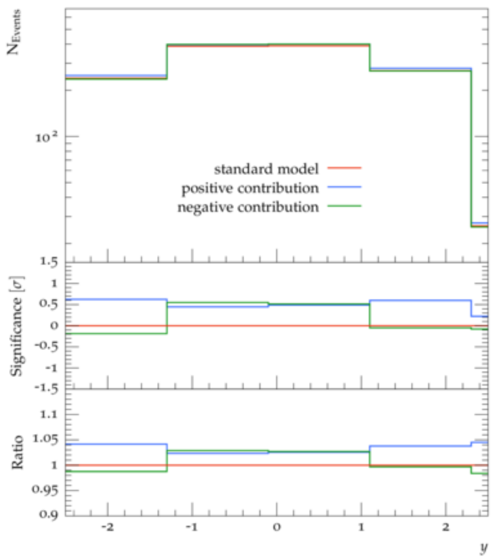

(c) $p_{T,\mathrm{Z}} \geq 100$ GeV, rebinned

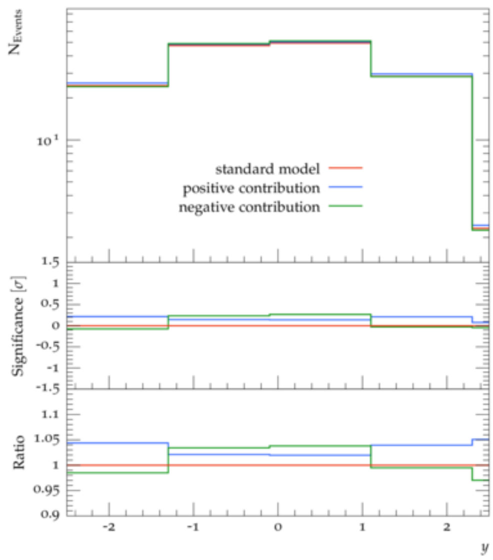

(d) $p_{T,\mathrm{Z}} \geq 200$ GeV, rebinned

Figure 5.5: Plots for the observable $y_{W\mathrm{Lepton}}$ of the $\mathcal{O}_{\varphi D}$ operator.

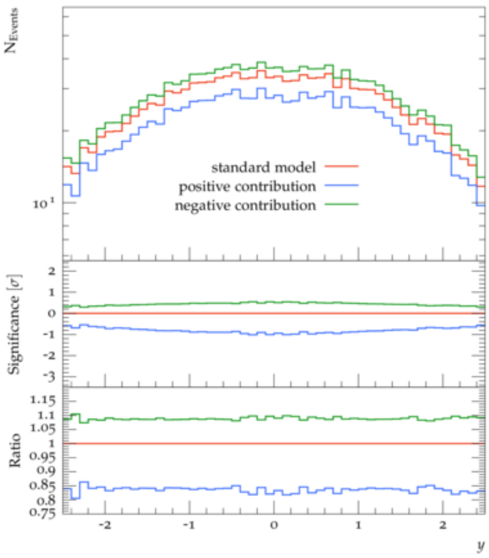

(a) $p_{T,\mathrm{Z}} \geq 100$ GeV

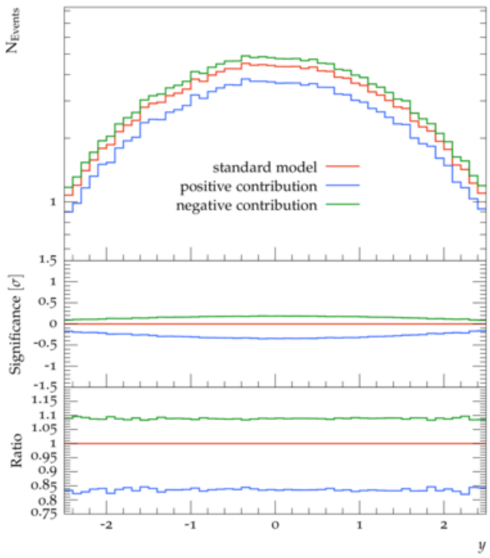

(b) $p_{T,\mathrm{Z}} \geq 200$ GeV

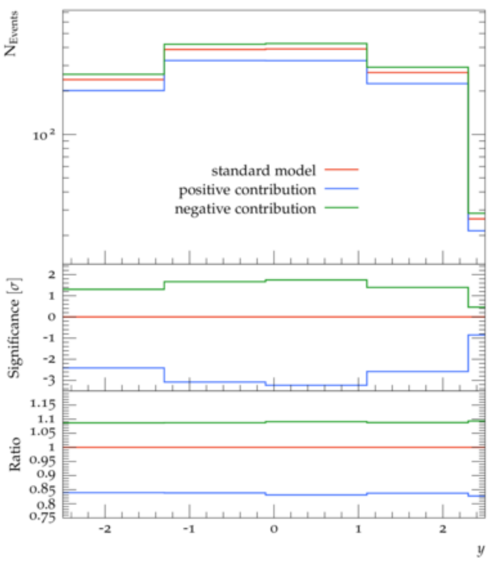

(c) $p_{T,\mathrm{Z}} \geq 100$ GeV, rebinned

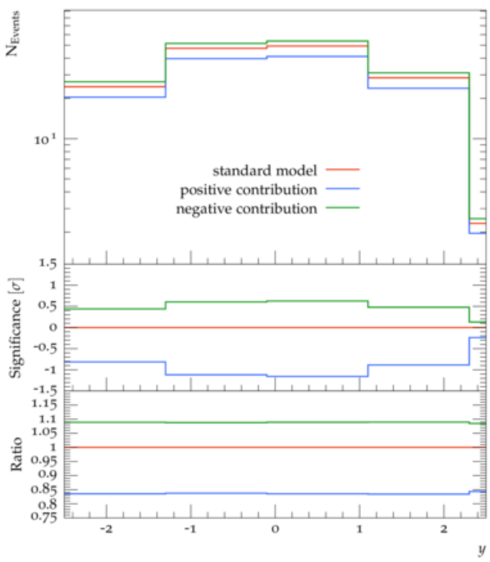

(d) $p_{T,\mathrm{Z}} \geq 200$ GeV, rebinned

Figure 5.6: Plots of the chosen observable for the fit of the $\mathcal{O}_{\varphi e}$ operator. The observable shown is $y_{W\ \mathrm{lepton}}$.

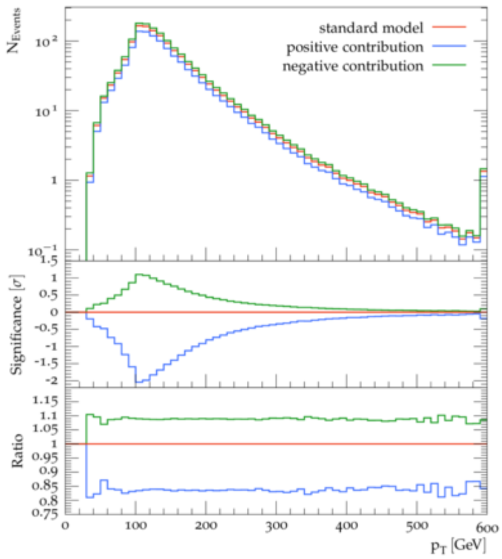

(a) $p_{T,\mathrm{Z}} \geq 100$ GeV

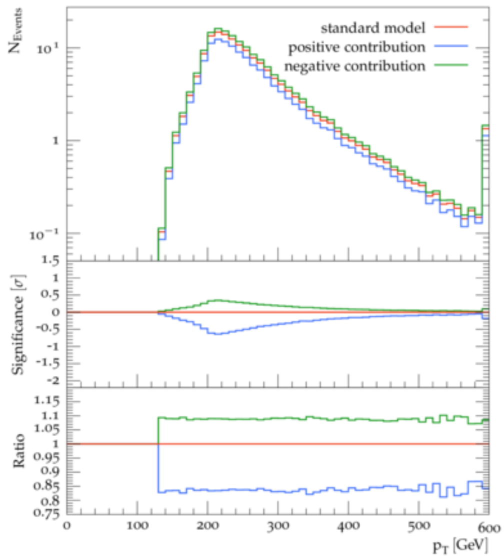

(b) $p_{T,\mathrm{Z}} \geq 200$ GeV

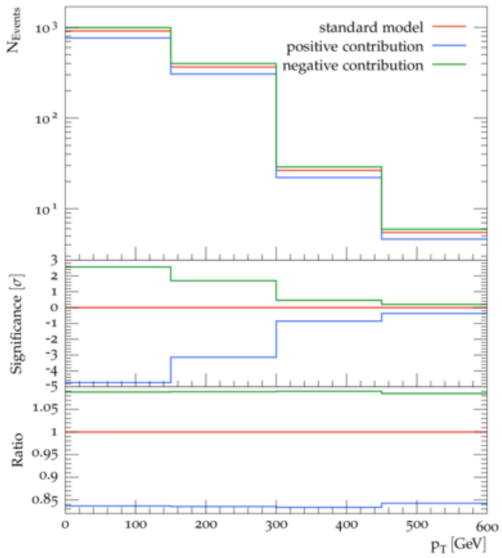

(c) $p_{T,\mathrm{Z}} \geq 100$ GeV, rebinned

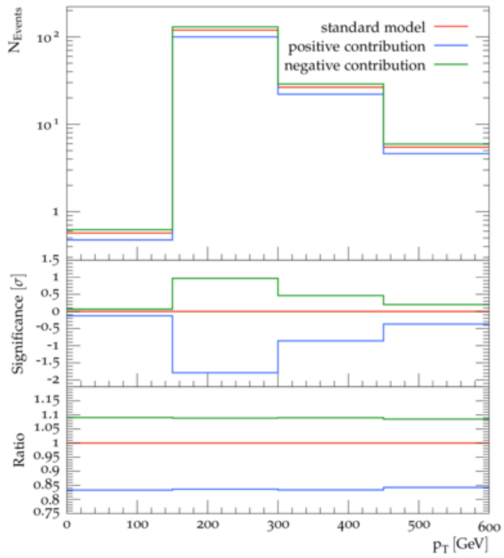

(d) $p_{T,\mathrm{Z}} \geq 200$ GeV, rebinned

Figure 5.7: Plots for the $p_{T,W}$ observable of the $\mathcal{O}_{\varphi e}$ operator.

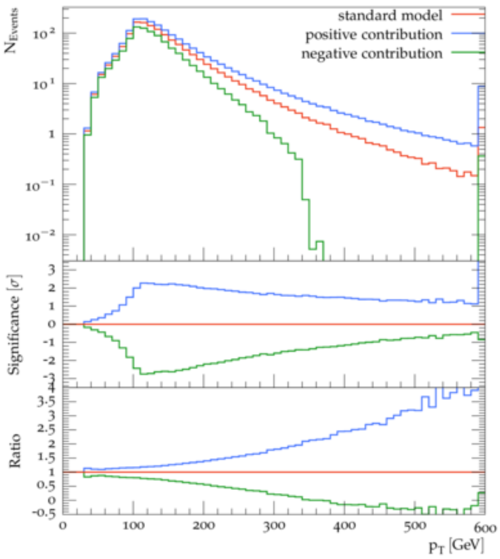

(a) $p_{T,\mathrm{Z}} \geq 100$ GeV

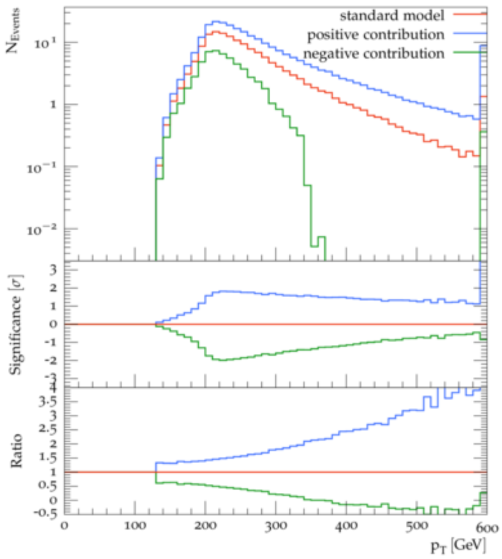

(b) $p_{T,\mathrm{Z}} \geq 200$ GeV

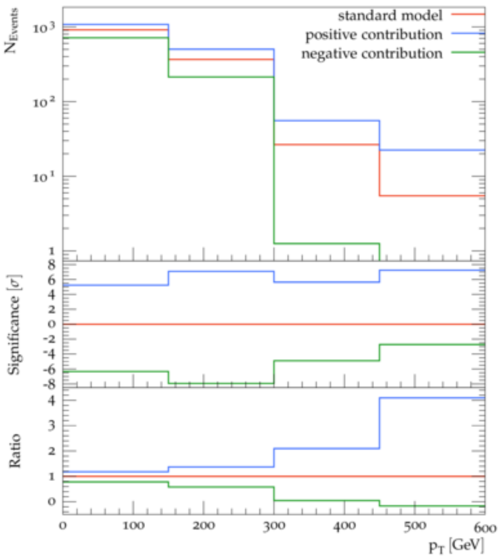

(c) $p_{T,\mathrm{Z}} \geq 100$ GeV, rebinned

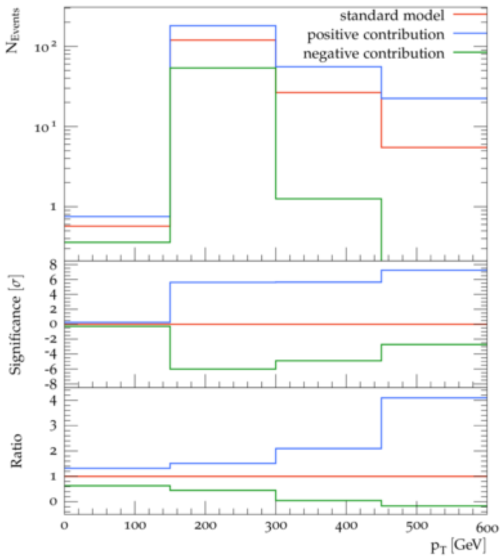

(d) $p_{T,\mathrm{Z}} \geq 200$ GeV, rebinned

Figure 5.8: Plots of the chosen observable for the fit of the $\mathcal{O}_{\varphi q3}$ operator. The observable shown is $p_{T,W}$.

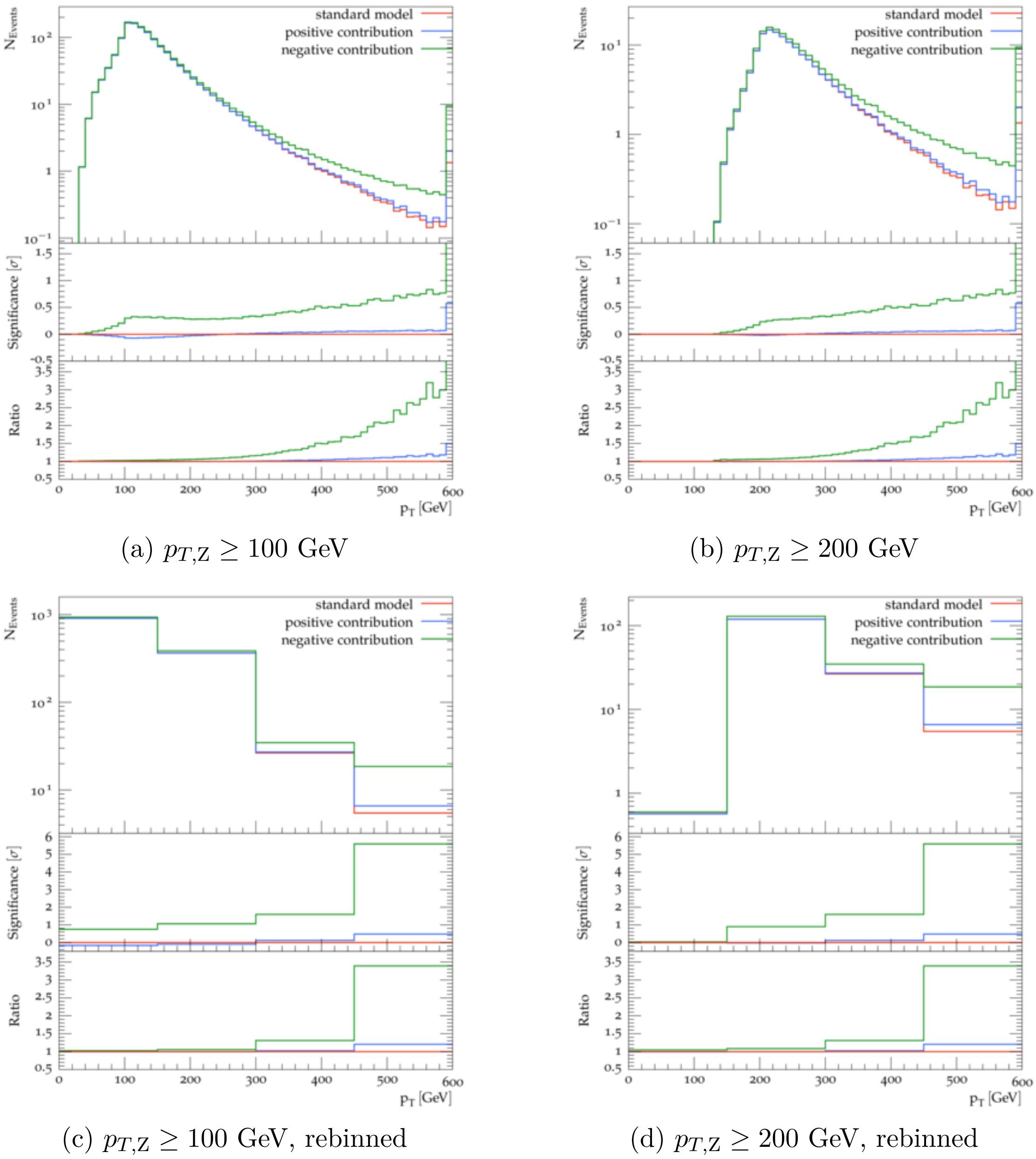

(a) $p_{T,\mathrm{Z}} \geq 100$ GeV

(b) $p_{T,\mathrm{Z}} \geq 200$ GeV

(c) $p_{T,\mathrm{Z}} \geq 100$ GeV, rebinned

(d) $p_{T,\mathrm{Z}} \geq 200$ GeV, rebinned

Figure 5.9: Plots of the chosen observable for the fit of the $\mathcal{O}_W$ operator. The observable shown is $p_{T,W}$.

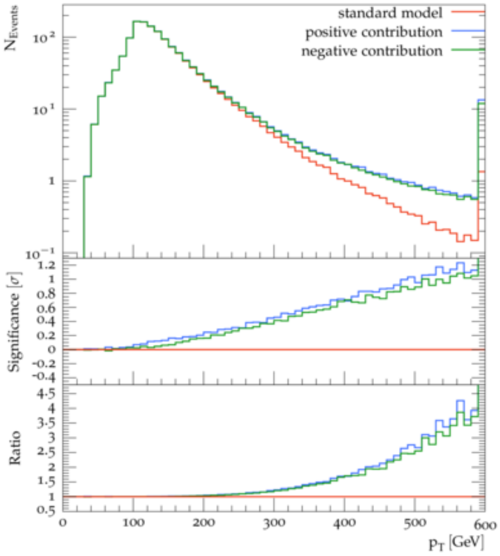

(a) $p_{T,\mathrm{Z}} \geq 100$ GeV

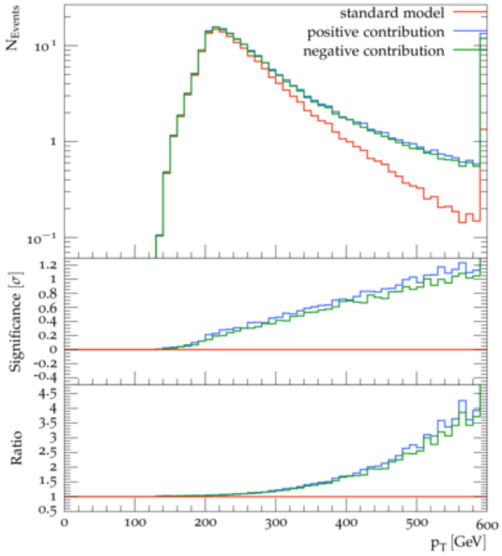

(b) $p_{T,\mathrm{Z}} \geq 200$ GeV

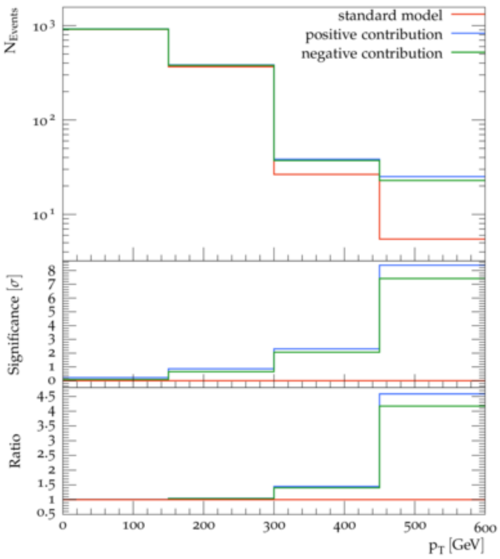

(c) $p_{T,\mathrm{Z}} \geq 100$ GeV, rebinned

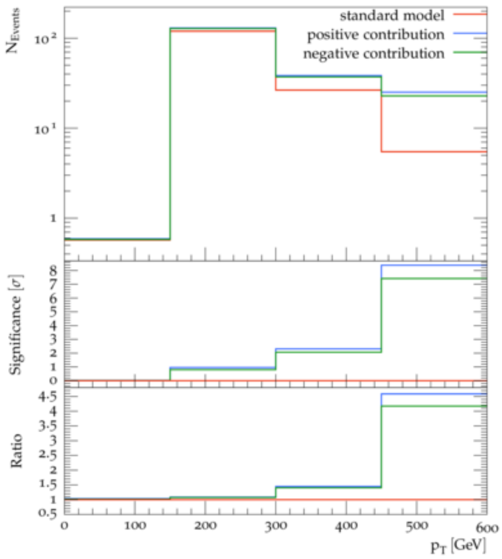

(d) $p_{T,\mathrm{Z}} \geq 200$ GeV, rebinned

Figure 5.10: Plots of the chosen observable for the fit of the $\mathcal{O}_{\tilde{W}}$ operator. The observable shown is $p_{T,W}$.

Table 5.1: Fit results for all studied operators compared to the old bound used in plotting. The $p_{T,Z} \geq 200$ GeV fit of the $\mathcal{O}_{\varphi l1}$ did not converge and no value could be found.

Operator	Cut	Old Bound		New Bound		Ratio to Old Bound	
		Lower	Upper	Lower	Upper	Lower	Upper
$\mathcal{O}_{\varphi D}$	$p_{T,Z} \geq 100$ GeV	-2.5	1.1	-7.0	2.0	2.8	1.8
	$p_{T,Z} \geq 200$ GeV	-2.5	1.1	-11	4.0	4.6	3.6
$\mathcal{O}_{\varphi e}$	$p_{T,Z} \geq 100$ GeV	-0.41	0.79	-1.5	2.9	3.6	3.6
	$p_{T,Z} \geq 200$ GeV	-0.41	0.79	-2.6	5.0	6.3	6.3
$\mathcal{O}_{\varphi l1}$	$p_{T,Z} \geq 100$ GeV	-0.23	0.098	-11	4.7	48	48
	$p_{T,Z} \geq 200$ GeV	-0.23	0.098	-	-	-	-
$\mathcal{O}_{\varphi l3}$	$p_{T,Z} \geq 100$ GeV	-0.29	0.1	-5.5	1.9	19	19
	$p_{T,Z} \geq 200$ GeV	-0.29	0.1	-9.5	3.3	33	33
$\mathcal{O}_{\varphi q1}$	$p_{T,Z} \geq 100$ GeV	-0.11	0.33	-0.32	0.79	2.9	2.4
	$p_{T,Z} \geq 200$ GeV	-0.11	0.33	-1.0	1.8	9.3	5.6
$\mathcal{O}_{\varphi q3}$	$p_{T,Z} \geq 100$ GeV	-0.14	0.11	-0.054	0.037	0.38	0.34
	$p_{T,Z} \geq 200$ GeV	-0.14	0.11	-0.076	0.045	0.54	0.41
$\mathcal{O}_{W}$	$p_{T,Z} \geq 100$ GeV	-0.15	0.04	-0.20	0.16	1.3	4.0
	$p_{T,Z} \geq 200$ GeV	-0.15	0.04	-0.35	0.10	2.3	2.5
$\mathcal{O}_{\tilde{W}}$	$p_{T,Z} \geq 100$ GeV	-0.17	0.18	-0.088	0.093	0.52	0.52
	$p_{T,Z} \geq 200$ GeV	-0.17	0.18	-0.088	0.093	0.52	0.52

6 Summary and Outlook

$W^{\pm}Z$ production connected to VB polarization is an active field of research in which BSM physics might be conceivably be observed. One way to look for BSM effects is the SMEFT approach for parameterizing deviations from the SM in high energy regions. In this thesis, SMEFT was used by looking at dimension six operators which contribute to the $W^{\pm}Z$ production process at LO and their effects in a phase space sensitive to VB polarization in quality and quantity were studied.
The phase space indeed seems to be sensitive to SMEFT contributions. A subset of operators - namely $\mathcal{O}_{\varphi q1}$, $\mathcal{O}_{\varphi q3}$, $\mathcal{O}_{W}$ and $\mathcal{O}_{\tilde{W}}$ - indeed showed qualitative shape effects and sensitivity in both angular as well as energy variables. Other operators did not indicate sensitivity beyond flat contributions. The fitting results of the operator in this VB polarization phase space have promising results. Even with comparatively basic binning it was possible to constrain the $\mathcal{O}_{\tilde{W}}$ and $\mathcal{O}_{\varphi q3}$ operators tighter compared to previous values. With further bin optimization it might be possible to set even tighter bounds on operators which are already tightly constrained by analyses from other phase spaces.
However, problems with the simulation in `SHERPA`, inconsistencies regarding the documented behaviour of propagator simulations compared to the actual simulation in light of the $\mathcal{O}_{\varphi D}$ contributions as well as inconsistencies during comparisons with similar studies done with different event generators require further investigations in the event generation setup and procedure used to generate and analyse the simulated events. On the one hand it is still not clear why certain operators do not give a hard process in `SHERPA` and why the operators that do, differ from the ones that `MadGraph` identifies as giving finite contributions. On the other hand the closure between different simulation methods of the EFT contributions is not reached, showing that the implementation of the SMEFT UFO models is not yet fully understood.
If the issues regarding the gauge loops are fixed, the operators which showed this issue might also be of interest for further study in this phase space. Further studies into the EFT effects on this phase space should also include the addition of

multiple operators simultaneously to see interference effects between combinations of two operators.

A Additional Plots and Discussions

Operators at Current Bounds

$\mathcal{O}_{\varphi l1}$

Similarly to $\mathcal{O}_{\varphi e}$, the $\mathcal{O}_{\varphi l1}$ operator shows next to no shape effect in Figure A.1. The ratio seems to stay at around 1.02 for the positive and 0.94 for the negative contribution.

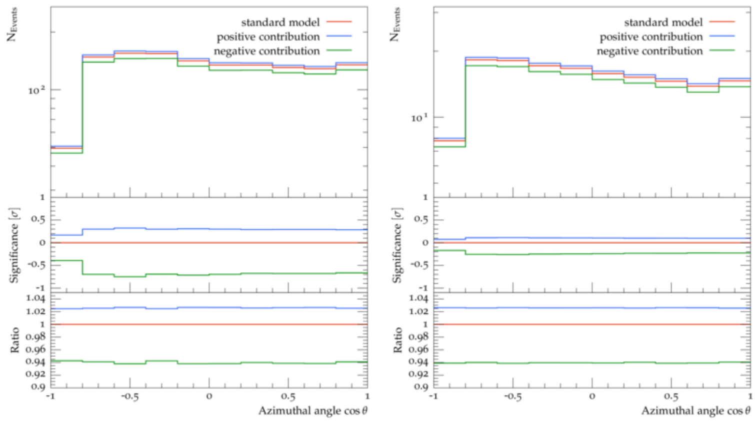

(a) $p_{T,\text{Z}} \geq 100$ GeV (b) $p_{T,\text{Z}} \geq 200$ GeV

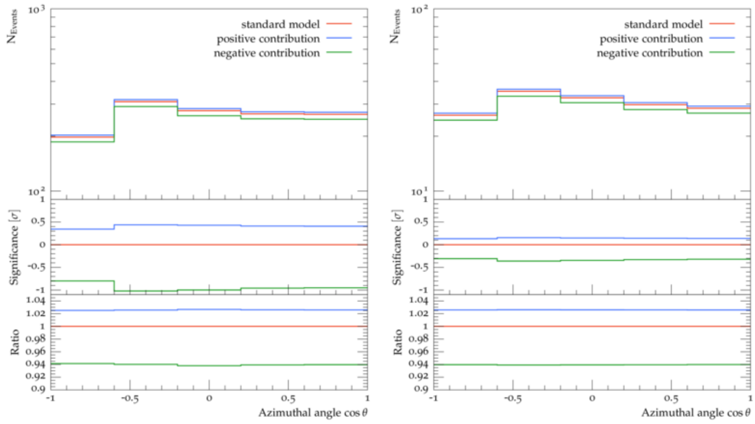

(c) $p_{T,\text{Z}} \geq 100$ GeV, rebinned (d) $p_{T,\text{Z}} \geq 200$ GeV, rebinned

Figure A.1: Plots of the chosen observable for the fit of the $\mathcal{O}_{\varphi l1}$ operator. The observable shown is $\cos\theta_{W\ \text{Lep}}^{\textbf{WZ into W}}$.

$\mathcal{O}_{\varphi l3}$

Similarly to $\mathcal{O}_{\varphi e}$ and $\mathcal{O}_{\varphi l1}$, the $\mathcal{O}_{\varphi l3}$ operator also shows next to no shape effect in Figure A.2. The ratio with respect to the SM seems to stay at around 1.15 for the positive and 0.95 for the negative contribution.

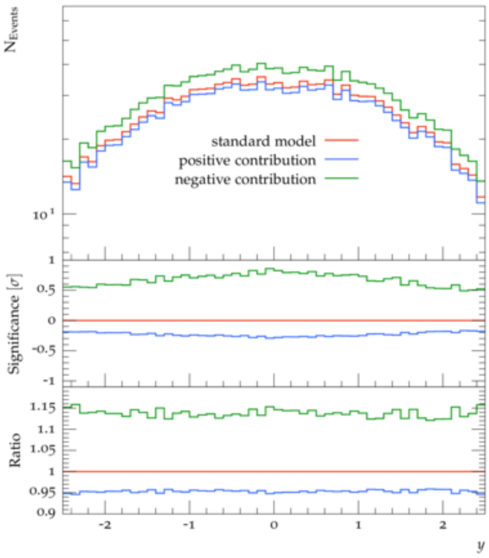

(a) $p_{T,\text{Z}} \geq 100$ GeV

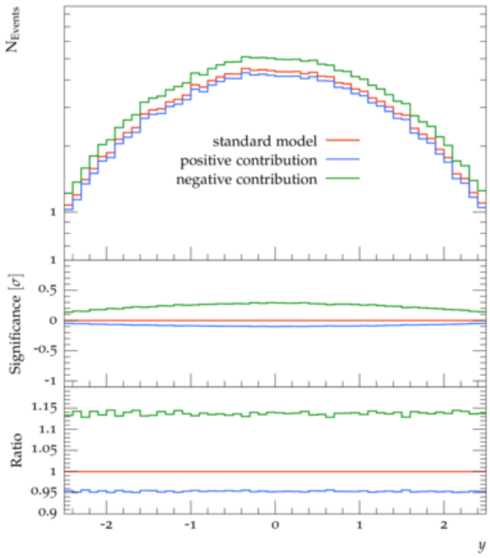

(b) $p_{T,\text{Z}} \geq 200$ GeV

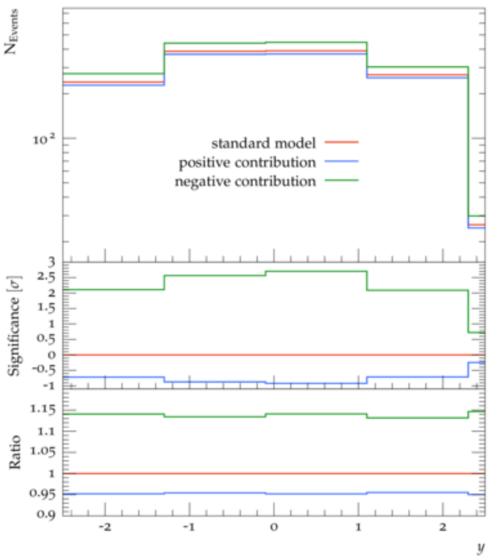

(c) $p_{T,\text{Z}} \geq 100$ GeV, rebinned

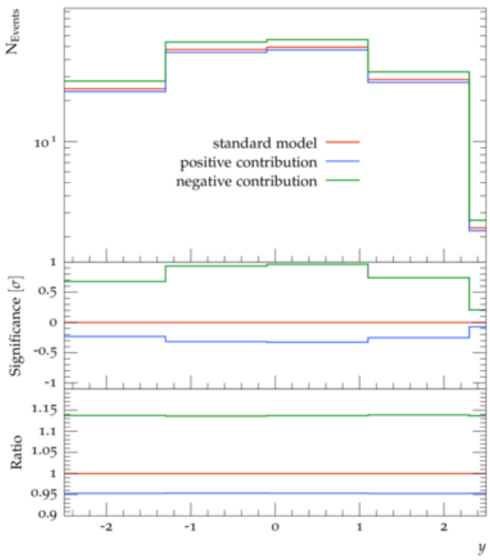

(d) $p_{T,\text{Z}} \geq 200$ GeV, rebinned

Figure A.2: Plots of the chosen observable for the fit of the $\mathcal{O}_{\varphi l3}$ operator. The observable shown is $y_{W\text{Lepton}}$.

$\mathcal{O}_{\varphi q1}$

Similarly to $\mathcal{O}_{\varphi D}$ a clear shape in the ratio plot is observed in both the higher binned and rebinned version of the observable plot in Figure A.3.

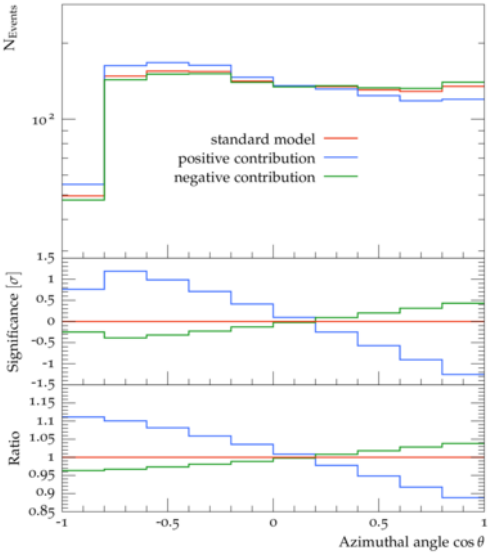

(a) $p_{T,\mathrm{Z}} \geq 100$ GeV

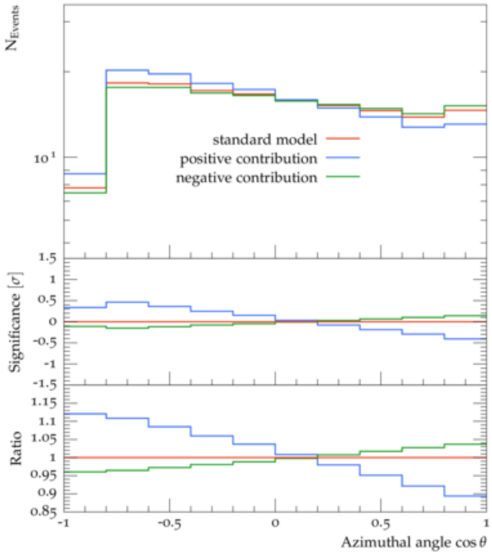

(b) $p_{T,\mathrm{Z}} \geq 200$ GeV

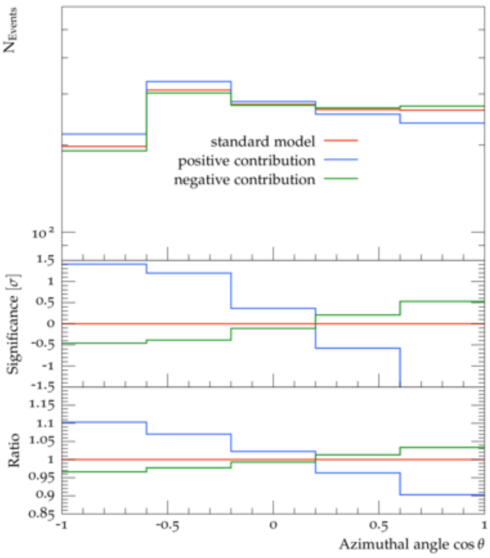

(c) $p_{T,\mathrm{Z}} \geq 100$ GeV, rebinned

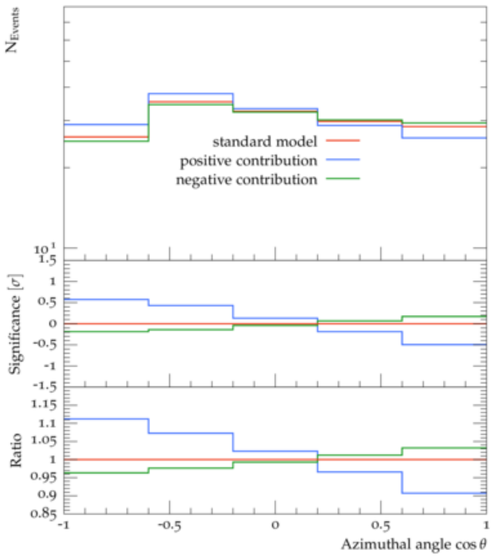

(d) $p_{T,\mathrm{Z}} \geq 200$ GeV, rebinned

Figure A.3: Plots of the chosen observable for the fit of the $\mathcal{O}_{\varphi q1}$ operator. The observable shown is $\cos\theta_{W\ \mathrm{Lep}}^{\mathbf{WZ\ into\ W}}$.

References

[1] ATLAS Collaboration. „Observation of a new particle in the search for the Standard Model Higgs boson with the ATLAS detector at the LHC". In: *Physics Letters B* 716.1 (Sept. 2012), pp. 1–29. DOI: 10.1016/j.physletb.2012.08.020. URL: https://www.sciencedirect.com/science/article/pii/S037026931200857X?via3Dihub.

[2] Paolo Girotti and. „Status of the Fermilab Muon $g-2$ Experiment". In: *EPJ Web of Conferences* 262 (2022). Ed. by P. Buehler and E. Widmann, p. 01003. DOI: 10.1051/epjconf/202226201003. URL: https://doi.org/10.1051.

[3] K. R. Labe. *The Muon g-2 Experiment at Fermilab*. 2022. arXiv: 2205.06336 [hep-ex].

[4] Mark Thomson. *Modern Particle Physics*. Cambridge University Press, 2013. ISBN: 978-1-107-03426-6.

[5] C. S. Wu et al. „Experimental Test of Parity Conservation in Beta Decay". In: *Phys. Rev.* 105 (4 Feb. 1957), pp. 1413–1415. DOI: 10.1103/PhysRev.105.1413. URL: https://link.aps.org/doi/10.1103/PhysRev.105.1413.

[6] G. Arnison et al. „Experimental Observation of Isolated Large Transverse Energy Electrons with Associated Missing Energy at $\sqrt{s}$ = 540 GeV". In: *Phys. Lett. B* 122 (1983), pp. 103–116. DOI: 10.1016/0370-2693(83)91177-2.

[7] G. Arnison et al. „Experimental Observation of Lepton Pairs of Invariant Mass Around 95-GeV/c**2 at the CERN SPS Collider". In: *Phys. Lett. B* 126 (1983), pp. 398–410. DOI: 10.1016/0370-2693(83)90188-0.

[8] Robert D. Klauber. *Electroweak Symmetry Breaking*. 2019. URL: http://www.quantumfieldtheory.info/Electroweak_sym_breaking.pdf.

[9] Kien Nguyen. *Electroweak Symmetry Breaking*. 2009. URL: https://www.theorie.physik.uni-muenchen.de/lsfrey/teaching/archiv/sose_09/rng/higgs_mechanism.pdf.

[10] R.L. Workman et al. (Particle Data Group). „Review of Particle Physics“. In: *Progress of Theoretical and Experimental Physics* 2022.8 (Aug. 2022). 083C01. ISSN: 2050-3911. DOI: 10.1093/ptep/ptac097. eprint: https://academic.oup.com/ptep/article-pdf/2022/8/083C01/49175539/ptac097.pdf. URL: https://doi.org/10.1093/ptep/ptac097.

[11] CMS Collaboration. „Measurement of the inclusive and differential WZ production cross sections, polarization angles, and triple gauge couplings in pp collisions at $\sqrt{s} = 13$ TeV“. In: *Journal of High Energy Physics* 2022.7 (July 2022). DOI: 10.1007/jhep07(2022)032. URL: https://link.springer.com/article/10.1007/JHEP07(2022)032.

[12] *Polarization settings in vector bosons.* URL: https://www.hep.phy.cam.ac.uk/~thomson/partIIIparticles/handouts/Handout_13_2011.pdf.

[13] ATLAS Collaboration. *Observation of gauge boson joint-polarisation states in $W^{\pm}Z$ production from pp collisions at $\sqrt{s} = 13$ TeV with the ATLAS detector*. 2022. arXiv: 2211.09435 [hep-ex].

[14] Cen Zhang. *Precision quest in interpretation: SMEFT at higher orders.* 2020. URL: https://indico.cern.ch/event/913339/contributions/3843897/attachments/2095378/3522057/smeft.pdf.

[15] Raquel Gomez-Ambrosio. „Studies of dimension-six EFT effects in vector boson scattering“. In: *The European Physical Journal C* 79.5 (May 2019). DOI: 10.1140/epjc/s10052-019-6893-2. URL: https://link.springer.com/article/10.1140/epjc/s10052-019-6893-2.

[16] B. Grzadkowski et al. „Dimension-six terms in the Standard Model Lagrangian“. In: *Journal of High Energy Physics* 2010.10 (Oct. 2010). DOI: 10.1007/jhep10(2010)085. URL: https://doi.org/10.1007.

[17] A. Dedes et al. „Feynman rules for the Standard Model Effective Field Theory in R_{ξ}- gauges“. In: *Journal of High Energy Physics* 2017.6 (June 2017). DOI: 10.1007/jhep06(2017)143. URL: https://link.springer.com/article/10.1007/JHEP06(2017)143.

[18] Juan Cristobal Rivera. *Studies of SMEFT in the WZ→lllv process.* 2023. URL: https://indico.cern.ch/event/1264450/contributions/5312603/attachments/2610593/4510295/SMEFT20studies20leptonic20WZ.pdf.

[19] Lyndon Evans and Philip Bryant. „LHC Machine“. In: *Journal of Instrumentation* 3.08 (Aug. 2008), S08001. DOI: 10.1088/1748-0221/3/08/S08001. URL: https://dx.doi.org/10.1088/1748-0221/3/08/S08001.

[20] Giles Chatham Strong. „On the impact of selected modern deep-learning techniques to the performance and celerity of classification models in an experimental high-energy physics use case“. In: *Machine Learning: Science and Technology* 1.4 (Sept. 2020), p. 045006. DOI: 10.1088/2632-2153/ab983a. URL: https://dx.doi.org/10.1088/2632-2153/ab983a.

[21] ATLAS Collaboration. „The ATLAS Experiment at the CERN Large Hadron Collider“. In: *Journal of Instrumentation* 3.08 (Aug. 2008), S08003. DOI: 10.1088/1748-0221/3/08/S08003. URL: https://dx.doi.org/10.1088/1748-0221/3/08/S08003.

[22] Alessandro La Rosa. *The ATLAS Insertable B-Layer: from construction to operation.* 2016. arXiv: 1610.01994 [physics.ins-det].

[23] Enrico Bothmann et al. „Event generation with Sherpa 2.2“. In: *SciPost Physics* 7.3 (Sept. 2019). DOI: 10.21468/scipostphys.7.3.034. URL: https://scipost.org/10.21468/SciPostPhys.7.3.034.

[24] *SMEFTsim_topU3l_MwScheme.* URL: https://github.com/SMEFTsim/SMEFTsim/tree/main/UFO_models/SMEFTsim_topU3l_MwScheme_UFO.

[25] *Sherpa 3.0.0 Manual.* URL: https://sherpa-team.gitlab.io/sherpa/master/index.html.

[26] *TAURUS TU Dresden HPC Cluster Documentation.* URL: https://doc.zih.tu-dresden.de/.

[27] Christian Bierlich et al. „Robust Independent Validation of Experiment and Theory: Rivet version 3“. In: *SciPost Phys.* 8 (2020), p. 026. DOI: 10.21468/SciPostPhys.8.2.026. URL: https://scipost.org/10.21468/SciPostPhys.8.2.026.

[28] T. Gleisberg et al. „Event generation with SHERPA 1.1“. In: *Journal of High Energy Physics* 2009.02 (Feb. 2009), p. 007. DOI: 10.1088/1126-6708/2009/02/007. URL: https://dx.doi.org/10.1088/1126-6708/2009/02/007.

[29] Ilaria Brivio, Yun Jiang and Michael Trott. „The SMEFTsim package, theory and tools“. In: *Journal of High Energy Physics* 2017.12 (Dec. 2017). DOI: 10.1007/jhep12(2017)070. URL: https://doi.org/10.1007/JHEP04(2021)073.

[30] Ilaria Brivio. „SMEFTsim 3.0 — a practical guide“. In: *Journal of High Energy Physics* 2021.4 (Apr. 2021). DOI: 10.1007/jhep04(2021)073. URL: https://link.springer.com/article/10.1007/JHEP04(2021)073.

[31] J. A. Aguilar Saavedra et al. *Interpreting top-quark LHC measurements in the standard-model effective field theory*. 2018. arXiv: 1802.07237 [hep-ph].

[32] *SHERPA issue regarding the Gauge Loop*. URL: https://gitlab.com/sherpa-team/sherpa/-/issues/464.

[33] Stefanie Todt. „The $W^{\pm}W^{\pm}$ Scattering Process – Theoretical Studies, Observation, Cross-section Measurement, and EFT Reinterpretation at $\sqrt{s} =$ 13 TeV with the ATLAS Detector“. Presented 02 Dec 2022. 2022. URL: https://cds.cern.ch/record/2845282.

[34] *Rivet analysis used for the generated events*. URL: https://gitlab.cern.ch/patmasid/rivetroutine_wz_00enhancedregion/-/blob/master/ATLAS_WZ_00enhanced_emu_latest.cc.

[35] *YODA Data analysis tool for RIVET analyses*. URL: https://yoda.hepforge.org/.

[36] J. Lambert. *WZ → lllv EFT Analysis: Rivet and EFT fit with EFTFun*. URL: https://indico.cern.ch/event/1271652/contributions/5339958/attachments/2624788/4538953/wz_group_meeting_April04-2.pdf.

[37] John Ellis et al. „Top, Higgs, diboson and electroweak fit to the Standard Model effective field theory“. In: *Journal of High Energy Physics* 2021.4 (Apr. 2021). DOI: 10.1007/jhep04(2021)279. URL: https://link.springer.com/article/10.1007/JHEP04(2021)279.

[38] *Combined effective field theory interpretation of differential cross-sections measurements of WW, WZ, 4l, and Z-plus-two-jets production using ATLAS data*. Tech. rep. Geneva: CERN, 2021. URL: https://cds.cern.ch/record/2776648.

[39] Thi Nhung Dao and Duc Ninh Le. *Enhancing the doubly-longitudinal polarization in WZ production at the LHC*. 2023. arXiv: 2302.03324 [hep-ph].

[40] Zhibo Wu, Fabrice Balli and Frederic Deliot. *Measurements of W and Z boson production in ATLAS*. Tech. rep. Geneva: CERN, 2022. DOI: 10.21468/SciPostPhysProc.8.031. URL: https://cds.cern.ch/record/2775636.

Erklärung

Hiermit erkläre ich, dass ich diese Arbeit im Rahmen der Betreuung am Institut für Kern- und Teilchenphysik ohne unzulässige Hilfe Dritter verfasst und alle Quellen als solche gekennzeichnet habe.

Gregor Daberstiel
Dresden, Mai 2023